universität wien

MASTERARBEIT / MASTER'S THESIS

Titel der Masterarbeit / Title of the Master's Thesis

„Investigation of heterogeneous nucleation of water vapor on airborne nanoplastic particles“

verfasst von / submitted by

Ruth Konrat, BSc

angestrebter akademischer Grad / in partial fulfilment of the requirements for the degree of

Master of Science (MSc)

Wien, 2023 / Vienna, 2023

Studienkennzahl lt. Studienblatt / degree programme code as it appears on the student record sheet:	UA 066 876
Studienrichtung lt. Studienblatt / degree programme as it appears on the student record sheet:	Masterstudium Physik
Betreut von / Supervisor:	Assoz. Prof. Dr. Paul Winkler, Privatdoz.

Acknowledgment

First of all, I would like to thank Prof. Winkler for giving me the opportunity to work in the lab. I'm especially grateful for being introduced in the scientific research and for enabling me to be part of a paper and therefore learning about the publishing process. Special thanks go out to Andreas Beier. When my laptop went haywire and all my codes didn't seem to work on my new one, Andi helped me immensely. Without him I would probably still try to make them run. Thanks to each member of the Aerosol group, for welcoming me and being part of this working group. Most of all, I would like to thank Peter Wlasits for his support whenever I have had any difficulties and for answering all of my questions. I'm going to cherish even the worst measurement days because somehow in the end they were still fun. And of course I'm especially grateful for every Mochi imported from Japan. Last but not least, I want to thank my family and friends, for supporting me with every step of the way. I thank my mother for her help that I can always rely on. Thanks to my father, for having to read this thesis over and over again. And of course, thanks to my older sister who is not only a great role model to lead the way but also a constant support in every situation in life.

Abstract

Clouds have an influence on the earth's radiation budget. However, the extent is still uncertain. In order to adequately account for the interaction between solar/terrestrial radiation and clouds, a deeper understanding of the formation of clouds is important. The initial step of cloud formation is heterogeneous nucleation. Clouds are formed in the atmosphere at supersaturation conditions and the formation is energetically favored if so-called seed particles are present. Besides the change in our climate, due to the emission of man-made greenhouse gases, the accumulation of plastic waste emerged as a big global problem. The serious consequences of this pollution on our health and the environment, especially because of the formation of microplastics and nanoplastics, have not been adequately researched. Within this thesis heterogeneous nucleation of water vapor on nanoplastic particles was investigated by the employment of the Size Analyzing Nuclei Counter (SANC). The sample nanoparticles were generated by evaporating bulk plastics in a tube furnace. The tested plastic was Polyethylene therephthalate (PET). Two different variants of this plastic type were studied: commodity PET retrieved from a plastic water bottle and chemical-standard PET. These two plastic types differ in their chemical composition. Plastics that we encounter in everyday life is assumed to be altered by additives. This commodity PET is compared to a "purer" version. The results show that differences in the chemical composition of PET have an influence on the nucleation behavior.

Zusammenfassung

Wolken haben einen großen Einfluss auf unser Klima, aber das genaue Ausmaß lässt sich bislang schwer einschätzen. Um die Auswirkungen adäquat beurteilen zu können, ist ein tief gehendes Verständnis der Prozesse ihrer Entstehung nötig. Wolken entstehen bei übersättigter Luft. Sind sogenannte Kondensationskeime vorhanden, ist ihre Ausbildung energetisch begünstigt. Dieser Prozess wird als heterogene Keimbildung bezeichnet. Neben der Veränderung des Klimas durch die Emission von Treibhausgasen vergrößert sich die Klimakrise aufgrund zusätzlicher Verschmutzung der Umwelt durch die Ansammlung von Plastikmüll. Die weitreichenden Folgen auf unsere Gesundheit und die Umwelt, vor allem durch die Entstehung von Mikroplastik und Nanoplastik, müssen daher genauer erforscht werden. In der vorliegenden Masterarbeit wird die heterogene Keimbildung von Wasserdampf an Nanoplastik mit Hilfe des Size Analyzing Nuclei Counter (SANC) untersucht. Die Testpartikel wurden durch die Verdampfung von Kunststoff in einem Röhrenofen hergestellt. Zwei Arten von Plastik (Polyethyleneterephthalat) unterschiedlicher Herkunft wurden untersucht: Haushaltsplastik von einer Plastikflasche und Plastik, welches für chemische Analysen verwendet wird. Diese beiden Plastikvarianten unterscheiden sich in ihrer chemischen Zusammensetzung (durch Zugabe unterschiedlicher Additive). In der vorliegenden Masterarbeit konnte gezeigt werden, dass eine unterschiedliche chemische Zusammensetzung der Plastikvarianten einen signifikanten Einfluss auf das Nukleationsverhalten hat.

List of Abbreviations

aci aerosol-cloud interaction.
ari aerosol-radiation interaction.

CAMS Constant Angle Mie Scattering.
CAS Chemical Abstracts Service.
CCN Cloud Condensation Nuclei.
CNT Classical Nucleation Theory.
CPC Condensation Particle Counter.
cPET commodity plastics.

DMA Differential Mobility Analyzer.
DMPS Differential Mobility Particle Sizer.

ERF Effective Radiative Forcing.

FCE Faraday Cup Electrometer.
FTIR Fourier Transform Infrared Spectroscopy.
FWHM Full Width at Half Maximum.

INP Ice Nucleating Particle.
IPCC International Panel on Climate Change.

MP microplastic.

NaCl sodium chloride, salt.
NP nanoplastic.

PE Polyethylene.
PET Polyethylene terephthalate.
PNSD Particle Number Size Distribution.
PP Polypropylene.
pPET plastics for chemical analysis.

RH Relative Humidity.

SANC Size Analyzing Nuclei Counter.

UCPC Ultrafine Condensation Particle Counter.

List of Symbols

ϵ_0	vacuum permittivity.
ϵ_l	permittivity of condensing liquid.
η	gas viscosity.
σ	surface tension.
θ	contact angle.
α	polarizability.
β	condensation coefficient.
β	expansion ratio.
β	resolution.
γ	evaporation coefficient.
$\hat{A}$	amplitude.
κ	adiabatic coefficient.
λ	mean free path.
$\mathcal{D}_p$	geometric particle diameter.
$\mathcal{S}$	entropy.
μ	chemical potential.
μ	mean value.
σ	standard deviation.
A	surface area of the cluster.
a_i	approximation coefficient.
A_{1-5}	coefficients for the calculation of saturation equilibrium vapor pressure.

C kinetic prefactor.

C_c Cunningham factor.

d dipole moment.

d_p particle diameter.

e elementary charge.

f shape factor.

f_c charge distribution.

G Gibbs free energy.

HV high voltage.

I net flow rate.

i number of molecules, number of charges.

I_e electric current.

J nucleation rate.

k Boltzmann factor.

L length of DMA.

l distance between two charges.

m contact parameter.

N particle number concentration.

n^* number of molecules in the critical cluster that are in excess of the number of molecules in the vapor phase occupying the volume of the critical cluster.

n_l number of molecules per unit volume of a liquid.

n_p number of charges per particle.

N_v number of molecules in the vapor phase.

p pressure.

q electric charge.

Q_a aerosol flow.

q_e flow rate of FCE.

Q_f flow rate through tube furnace.

Q_s sample flow.

Q_{dil} dilution flow rate.

Q_{ex} exhaust flow.

Q_{sh} sheath flow.

R radius of electrode.

r particle radius.

S saturation ratio.

T temperature.

t time.

U internal energy.

V voltage, volume.

V_{1-6} magnetic valves.

Z mobility.

Contents

1 | Introduction

Motivation

In 1990 the first IPCC report was published, emphasizing climate change and its potential challenges [1]. Since then, an increasing number of reports and studies confirm the undeniable influence of mankind on the climate and the average global warming effect.

Effective Radiative Forcing (ERF) is a common measure to access the influence of contributors on the climate. ERF is the change in the energy budget of the earth, given in watts per square meter [2]. A positive value of the ERF indicates a gain in energy, respectively an increase in surface temperature, while a negative value describes the loss of energy (decrease of surface temperature) [3]. In Figure 1.1 a summary of the most common contributors is given with their effective radiative forcing. This graphic clearly shows that most antropogenic contributors have a warming effect on the earth's system with the exception of aerosols and clouds. In addition, these factors are also the contributors with the highest uncertainties. The influence of aerosols on the climate can be divided in aerosol-cloud interaction (aci) and aerosol-radiation (ari) interaction [2]. The aerosol-radiation interaction describes the scattering and absorption of radiation by aerosol particles [4]. Aerosol-cloud interaction covers the influence of aerosol particles on the properties of clouds and their formation via nucleation, since aerosol particles can act as cloud condensation nuclei (CCN) [5]. Aerosols and clouds have a mainly cooling effect but the magnitude of this influence is fraught with uncertainties [5]. To improve climate models and to predict how the warming effect changes the formation of clouds, we need to understand atmospheric nucleation mechanisms. In order to properly account for the effects of clouds, the micro-physical properties that describe the influence of aerosols on the formation of clouds need to be fully understood.

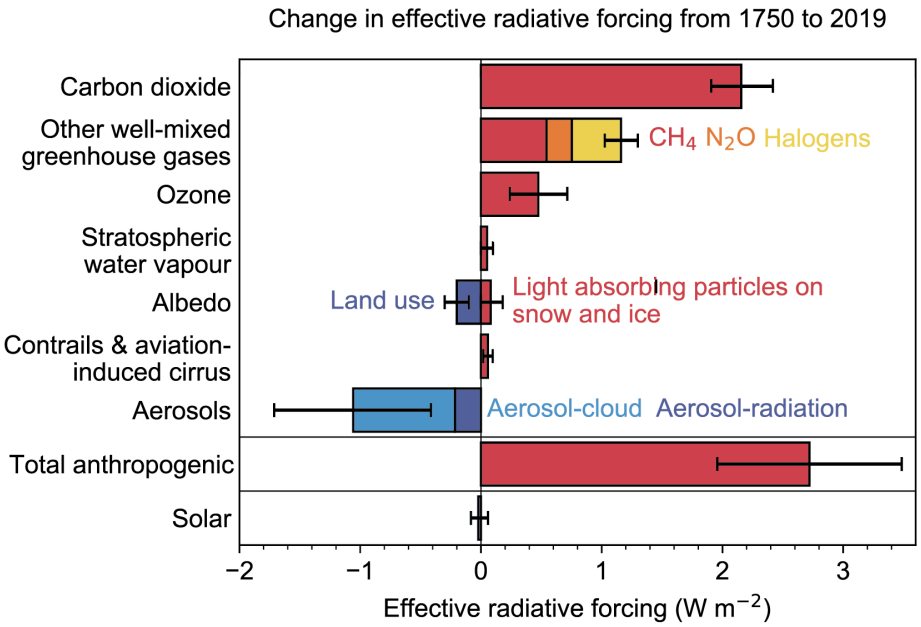

Figure 1.1: Comparison of the effective radiative forcing (ERF) for different contributors including uncertaincy bars [6].

Atmospheric particle formation and cloud formation

Aerosols are liquid or solid particles that are suspended in a gas [5]. There is a distinction between so-called primary and secondary particles. The former describes particles that are emitted into the atmosphere, whereas the latter are particles that are being formed by gas-to-particle conversion [7]. Particle formation within the atmosphere is based on nucleation, which is the initial step necessary for the transition into a new phase [8]. Prerequisite for nucleation processes is supersaturated vapor [9]. If seed particles are present, nucleation becomes energetically more favorable, which leads to heterogeneous nucleation [10]. Without seed particles higher supersaturation is needed for so-called homogeneous nucleation to be initiated which usually does not occur under atmospheric conditions [10].

Independent of the origin, once aerosol particles are in the atmosphere they can grow by either coagulation or condensation [7]. The latter is important for cloud formation. Figure 1.2 shows schematically the formation of clouds. Water vapor and seed particles of different sizes are present in supersaturated air (e.g. achieved by rising air which expands and cools) [5]. Clusters of water molecules are then formed on the seed particles. Following condensational growth, this ensemble of water droplets in the atmosphere leads to the formation of a cloud. These seed particles, promoting cloud formation, are so-called cloud condensation nuclei (CCN) [5].

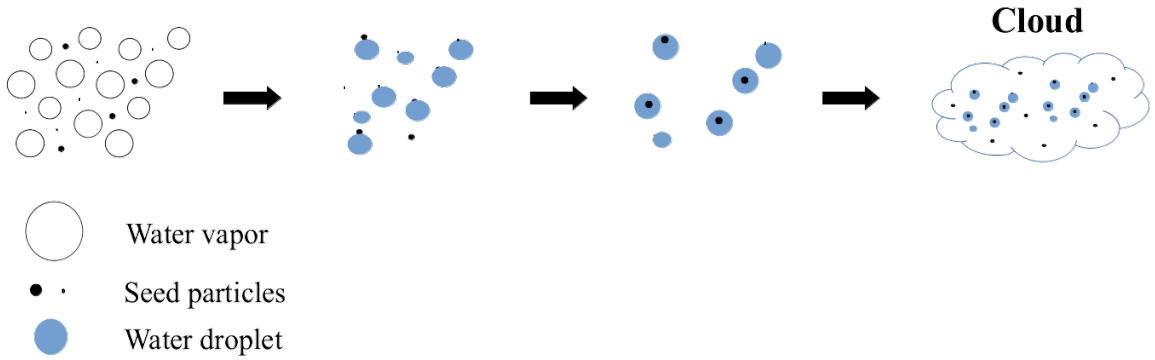

Figure 1.2: Illustration of heterogeneous nucleation; cluster formation, condensational growth and ultimately (liquid) cloud formation, based on [11]. The dimensions of the illustration are not to scale.

Clouds can be classified not only based on their altitude and form, but also in respect to their micro-physical properties [12]. Three different types can be distinguished, depending on the aggregation state: warm/liquid clouds (liquid phase), ice clouds (solid phase, ice crystals) and mixed-phase clouds (liquid and solid ice crystals) [12]. The freezing of cloud droplets to ice crystals or the formation of water vapor directly to ice crystals is called ice nucleation and can take place homogeneously or heterogeneously [13]. In the latter case ice nucleation particles (INPs) are present promoting the formation of ice crystals. Common INPs are solid insoluble particles such as mineral dust [13].

As mentioned, aerosol particles interact with solar radiation by absorption and scattering (ASI), influencing the earth's radiation budget [2]. Figure 1.3 demonstrates the interaction between incoming solar radiation and clouds as well as infrared radiation from the earth's surface [14]. The earth's climate depends on the balance between the incoming solar radiation (shortwave) and thermal outgoing radiation (longwave). Therefore changes in cloud properties have an effect on the cloud-climate feedback [14]. Aerosol particles can alter cloud properties by acting as CCNs and INPs. For instance, a higher concentration of CCNs or INPs at the same water content leads to a higher number of cloud droplets which are smaller in size, resulting in increased cloud albedo [15]. Furthermore, smaller cloud droplets decrease the possibility of collision, thereby slowing down precipitation, with the effect that the cloud's lifetime is increased [16].

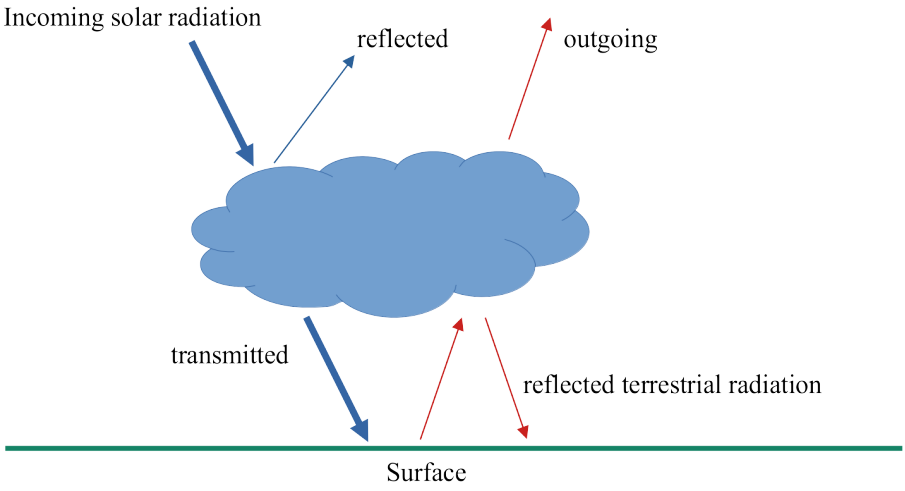

Figure 1.3: (Solar/terrestrial) radiation cloud interaction, adapted from [17], [14]. blue arrows indicate shortwave radiation, red arrows denote longwave radiation.

Degradation of plastic waste

Manmade influences on the environment are not only limited to the emission of greenhouse gases. The accumulation of plastic waste in oceans and the atmosphere constitutes a major threat to the environment.

Based on the definition of M. Vert et al. (2012, S.394) plastic is a "generic term describing polymeric material that may or may not contain other substances to improve performance and/or reduce costs" [18]. The first completely synthetic plastic was introduced by Leo Hendrick Baekerland in 1907 [19]. This newly developed material revolutionized modern life due to its versatile use [19]. The popularity of this material is manifold: low cost in production, ease of manufacture and resistance to temperature, light and water etc. [20]. Nowadays life without plastics would be unimaginable [21]. However, the negative side effects outdo the once so perfect image. The low degradation rates and its widespread use unavoidably result in an accumulation in the environment [22]. The fragmentation from bulk plastic into nanoplastic (NP) and microplastic (MP) can be animated by physical, chemical, biological stress or most likely a combination of these processes [23]. A strict definition of nanoplastic and microplastic is not yet available [20]. Overall a classification based on the size of the fragmented particles is suggested. However, the upper and lower limit for nanoplastics and microplastics vary. For example, nanoplastics can range from 1nm-100nm or up to 1000nm, depending on different authors [20].

First reports about the presence of micro-sized (smaller than 5mm) plastic particles in oceans were already reported in 1970, while terrestrial and mainly atmospheric studies remain scarce [24], [25]. A first evidence that microplastic is present even in remote environments was shown by A.R. Aves [26]. Herein, snow samples in Antartica were analyzed, with the result that microplastic was present in each sample with a long-range transportation up to 6000km corresponding to an estimated residence time of 6.5 days [26].

Until now, only the term "plastics" was mentioned. However, there is a classification for this term depending on the type of material and the constituents that were used in its production [27]. In general, there are two categories of polymeric products: thermosets and thermoplastics [28]. They differ in their reaction to heat exposure. While thermoplastics can undergo multiple heating and cooling cycles where they would get malleable, thermosets are resistant to heat [28]. Most commonly known thermoplastics are inter alia: Polyethylene (PE), Polypropylene (PP), Polyethylene terephthalate (PET) [29]. Each of these plastic types have various usages due to different properties concerning their flexibility, resistance to chemicals/solvents, hardness, transparency and resistance to heat for instance [27].

For this thesis the sole focus will be PET, as this type of polymeric material is mostly present in bottles, packaging or textile fibers [30]. Evidently, one of the most used materials among plastics. Furthermore, it allows stable generation of particles for reproducible studies [31]. Although this thesis is a prototypical study, similar effects can be anticipated for other plastic types.

2 | Theoretical Background

Nucleation phenomena are widely spread in various scientific domains, e.g. chemistry, physics, biology, atmospheric science [32]. In general, nucleation is the initial step of a phase transition [8]. The formation of a new stable phase does not occur spontaneously as new clusters are formed that need to overcome an energy barrier [33]. In the following, the phase transition between the vapor and the liquid phases will be discussed based on classical nucleation theory (CNT). The standard choice of describing the formation of a new cluster in nucleation processes is the Gibbs free energy G [34]:

$$G = U + pV - T\mathcal{S} \tag{2.1}$$

with internal energy U, pressure p, volume V, temperature T and entropy $\mathcal{S}$. Nucleation is accompanied with a change of Gibbs free energy dG. Differentiating eq.(2.1) and considering the first law of thermodynamics (dU = Td$\mathcal{S}$ - pdV) [35] leads to the following expression of dG:

$$dG = V\,dp - \mathcal{S}dT \tag{2.2}$$

According to eq.(2.2) for a system in equilibrium at constant T and p, G is stationary and takes in fact a minimum (dG = 0) [36].

2.1 Saturation Ratio

Considering an enclosed system where two phases (liquid and vapor phase) are coexisting, liquid molecules can be transferred to the vapor phase by evaporation and vapor molecules can enter the liquid phase by condensation [35]. If overall these transfers are balanced in both directions, the system is said to be in equilibrium [36]. This equilibrium state can be described by the difference in chemical potentials of the liquid μ_l and the vapor μ_v phases. The chemical potential is given as the Gibbs free energy per number of molecules of the substance [35]. A difference in chemical potential describes the direction in which a phase change takes place [35]. In case the system is in equilibrium, this difference is equal to zero. Rewriting the change in Gibbs free energy, eq.(2.2), in terms of the chemical potential and considering an

isothermal process (dT = 0) leads to the expression [37],[35]:

$$\frac{dG}{N_v} = d\mu_v = \frac{V}{N_v} dp$$

$$\xrightarrow{\text{ideal gas eq.}} \int_{\mu_v^{eq}=\mu_l}^{\mu_v} d\mu_v = \int_{p_S(T)}^{p} \frac{kT}{p} dp \tag{2.3}$$

After integrating eq.(2.3), the difference in chemical potential between the vapor and the liquid is given as [38]:

$$\Delta\mu = \mu_v - \mu_l = k\,T\,ln\left(\frac{p_v}{p_S(T)}\right) \tag{2.4}$$

The saturation ratio S follows from the ratio between the partial vapor pressure p_v over the saturation vapor pressure p_S(T) [37]:

$$S = \frac{p_v}{p_S(T)} \tag{2.5}$$

In a mixture of gases, the partial vapor pressure is the pressure exerted by one gas if it were present only by itself in the volume of the mixture [10]. The pressure that is needed to maintain a vapor in equilibrium with the condensed phase at a given temperature is called saturation vapor pressure, respectively equilibrium vapor pressure. [10]. Combining eq.(2.4) and eq.(2.5) leads to the final expression:

$$\mu_v - \mu_l = k\,T\,lnS \tag{2.6}$$

Considering eq.(2.6) three cases can be distinguished:

- $\mu_v < \mu_l$: the chemical potential of the liquid is bigger than the chemical potential of the vapor (equivalent to S $<$ 1); vapor is under-saturated and liquid droplets will evaporate until reaching the equilibrium [34]

- $\mu_l = \mu_v$: if the chemical potentials are equal, the difference is zero, leading to a saturation ratio of S = 1. This case describes the equilibrium state, where evaporation equals condensation

- $\mu_v > \mu_l$: the chemical potential of the vapor is bigger than the chemical potential of the liquid, the vapor is supersaturated (S $>$ 1), and condensation will predominantly take place [35]

2.2 Classical Nucleation Theory

The classical nucleation theory (CNT) is an approximation describing nucleation phenomena [39]. It convinces by its simplicity as it is based on general thermodynamics [34]. Bulk properties, (e.g. surface tension, density) are assumed for nano-sized clusters [9]. Two different nucleation processes have to be distinguished: Homogeneous and heterogeneous. The latter considers the presence of nuclei or ions, which facilitates nucleation [10].

Homogeneous Nucleation

The chemical potential μ is given as Gibbs free energy per molecule [35]. The Gibbs free energy G_i of a cluster with i molecules is greater than $\mu \cdot i$ since a surface term needs to be added, leading to the following expression for the cluster energy G_i [36]:

$$G_i = i \cdot \mu_i + A_i \cdot \sigma \tag{2.7}$$

The formation of a cluster consisting of i molecules is given by the nucleation work and is formulated by a change in Gibbs free energy [33]:

$$\Delta G_i = G_i - i\mu_v = \underbrace{G_i - i\mu_l}_{\substack{\text{excess free} \\ \text{energy}}} - i \underbrace{(\mu_v - \mu_l)}_{\text{eq.(2.4)}} \tag{2.8}$$

Eq.(2.7) and eq.(2.8) show that the excess free energy is only sensitive to the surface energy [33]. The number of molecules i with the assumption of a spherical cluster is given as [38]:

$$i = \frac{4\pi}{3} r_i^3 n_l \tag{2.9}$$

n_l is the specific density of the liquid, i.e. the number of molecules per unit volume [36]. Eq. (2.9) and eq.(2.8) lead to the final expression for the nucleation work, respectively the change in Gibbs free energy for the transition from the vapor to the liquid phase [33]:

$$\Delta G(r_i) = \underbrace{4\pi r_i^2 \sigma}_{\text{surface term}} - \underbrace{\frac{4\pi}{3} r_i^3 \, n_l \, k \, T \, lnS}_{\text{volume term}} \tag{2.10}$$

As already mentioned, supersaturation is necessary for the initiation of nucleation. In Figure 2.1 the nucleation work, eq.(2.10), as a function of the cluster size r is plotted for three different values of S. For S = 1 and S < 1, the nucleation work is positive and increases with increasing r, meaning that the formed clusters are unstable since evaporation is more likely [33]. In the case of supersaturation (S>1), we can identify from eq.(2.10) that the surface and the volume term are competing against each other. For smaller r, the surface term is more

dominant until the volume term takes over, which leads to a maximum of ΔG (energy-barrier) [33]. This maximum is reached at the critical cluster radius r*. For sizes smaller than the critical radius, clusters will most likely evaporate without the formation of a new phase [33]. However, once this critical radius is reached, the growth of the clusters are energetically more favourable than their evaporation [34].

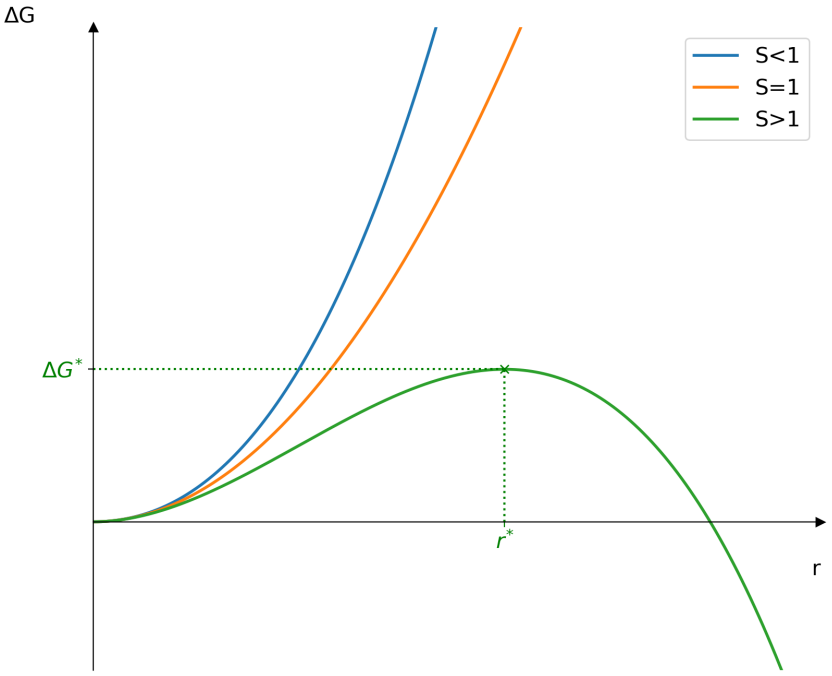

Figure 2.1: Schematic behavior between the nucleation work ΔG and the cluster radius r for three different saturation ratio values; an energy-barrier that can be surmounted by a cluster is only present for S > 1. r* is called the critical radius. Beyond this size, clusters are more likely to grow than to vanish [34].

The extreme value at r* can be calculated by differentiating eq.(2.10) and equating to zero, which leads to the Kelvin equation [38]:

$$r^* = \frac{2\sigma}{n_l\, k\, T\, lnS} \tag{2.11}$$

with corresponding nucleation work:

$$\Delta G^*(r^*) = \frac{4\pi}{3}\sigma r^{*2} = \frac{16\pi\,\sigma^3}{3(n_l\, k\, T\, lnS)^2} \tag{2.12}$$

Exceeding the value S=1 enables the formation of clusters. Figure 2.2 demonstrates the dependence of the energy barrier and the saturation ratio: The greater the saturation ratio, the smaller the energy barrier. From the same figure it can also be concluded that for a smaller energy barrier (ΔG_2^*) the size of the critical cluster (r_2^*) is smaller as well. Consequently,

nucleation is increasingly likely with increasing S.

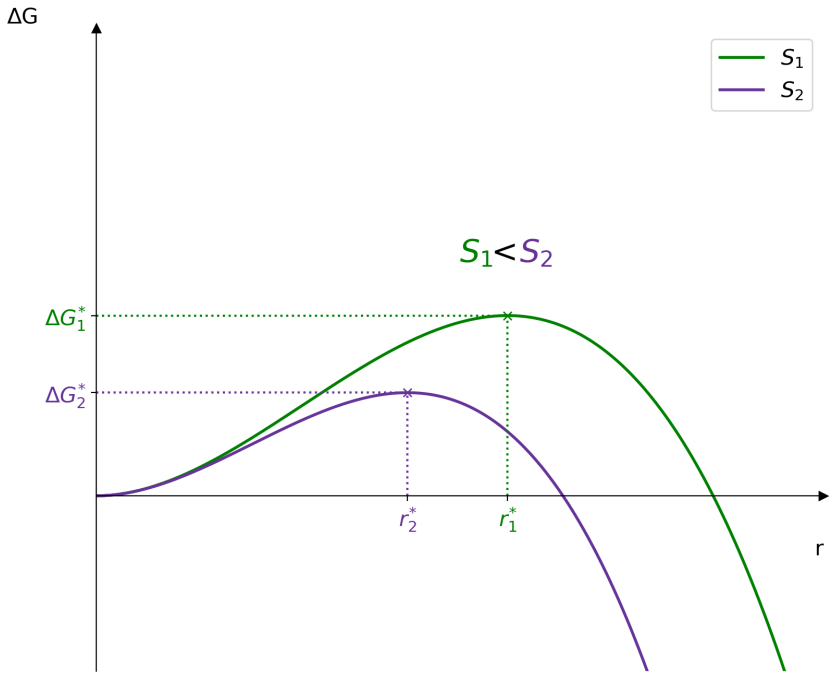

Figure 2.2: Comparison of different magnitudes of S, showing that a higher supersaturation reduces the energy barrier and the critical cluster size.

2.2.1 Kinetic Approach

The condensation of molecules to a cluster as well as the evaporation are statistical processes that can be described by rate equations [9]. Considering a cluster with i molecules (also called monomers) gaining of additional molecules leads to growth and losing of molecules to shrinkage of the cluster [9]. The addition of monomers to the cluster is described by the condensation coefficient β and the loss of monomers by the evaporation coefficient γ [9]. The net flow rate I(i) to a cluster of size i is given by [8]:

$$I(i) = \beta(i) \cdot N(i) - \gamma(i+1) \cdot N(i+1) \tag{2.13}$$

The change in cluster concentration N containing i molecules over time t is described by the so-called birth-death equation [9]:

$$\begin{aligned} \frac{dN(i)}{dt} &= \beta(i-1) \cdot N(i-1) - \gamma(i) \cdot N(i) - \beta(i) \cdot N(i) + \gamma(i+1) \cdot N(i+1) \\ &= I(i-1) - I(i) \end{aligned} \tag{2.14}$$

As depicted in Figure 2.3 the time-dependent concentration to a cluster size i is positively influenced by the contribution of β(i-1) · N(i-1) and γ(i+1) · N(i+1). Losses of the concentration occur because of the evaporation (γ(i) · N(i)) and the condensation to cluster size $i+1$ (β(i) · N(i)). [9]

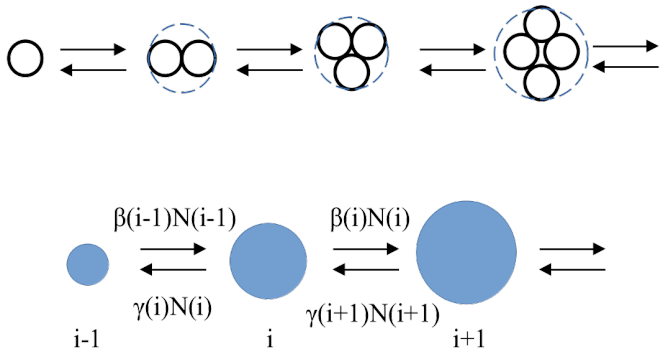

Figure 2.3: Schematic representation of growth and shrinkage of a cluster by gaining or losing molecules, based on [9].

The cluster concentration N(i) does not change in a steady-state, meaning that eq.(2.14) = 0, leading to one flux rate [8]:

$$I(i-1) = I(i) = ... = I(i+1) =: J\left[\frac{1}{cm^3 s}\right] \tag{2.15}$$

J is the so-called nucleation rate. This steady-state describes the size independence of the flow. The nucleation rate for the formation of the critical cluster has the following form, where C is a kinetic prefactor [34]:

$$J = C \cdot exp\left(-\frac{\Delta G^*}{kT}\right) \tag{2.16}$$

This prefactor C is dependent on β, the Zeldovich factor Z and the number of monomers in the nucleating vapor [40]. The Zeldovich factor takes into consideration that the nucleating vapor is not in equilibrium and accounts for the fact that clusters larger than the critical size can decay back [8], [34].

Heterogeneous Nucleation

In contrast to homogeneous nucleation, heterogeneous nucleation describes the case where nucleation occurs on a surface [10]. Considering a flat insoluble surface where liquid droplets can nucleate on, the nucleation work can be described similarly to the homogeneous case but with the multiplication by a geometric factor f [8]:

$$\Delta G^{het*} = f(m) \cdot \Delta G^{hom*} \tag{2.17}$$

This factor is dependent on the contact parameter m [38]:

$$f(m) = \frac{(2+m)\cdot(1-m)^2}{4} \tag{2.18}$$

The contact parameter m is given by Young's equation eq.(2.19), where θ is the so-called macroscopic contact angle [41]. This angle is expressed by the interfacial tensions (σ) between the vapor (v), solid (s) and liquid (l).

$$m = cos(\theta) = \frac{\sigma_{sv} - \sigma_{sl}}{\sigma_{lv}} \tag{2.19}$$

The contact angle can be seen as a concept of describing the wettability of a surface [13], where small angles represent good wettability. The minimal case of $\theta = 0°$ corresponds to full wetting. Herein the cluster completely wraps around the surface. θ can take on values from 0° to 180°. Consequently, it holds that $0 < f_G < 1$, meaning that the presence of a surface reduces in most situations the energy barrier [38]. Figure 2.4 show that smaller nucleation work is needed for the heterogeneous case than for the homogeneous case.

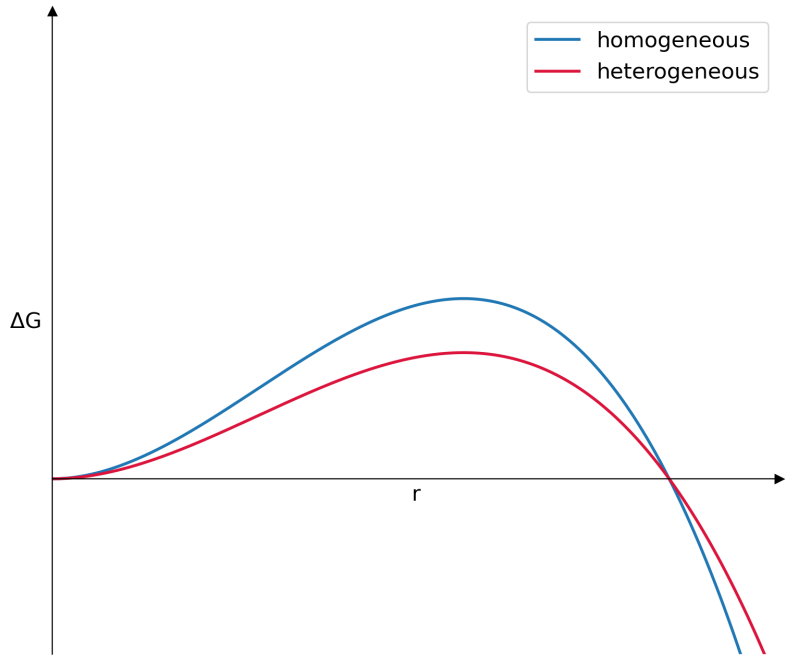

Figure 2.4: Comparison of Gibbs free energy in the case of heterogeneous (f(m) = 0.7) and homogeneous nucleation.

The nucleation rate for heterogeneous nucleation is given by:

$$J_{het} = C_{het} \cdot exp\left(-\frac{\Delta G^*_{het}}{kT}\right) \tag{2.20}$$

Herein, the prefactor is given by the Zeldovich factor Z_{het}, the rate that vapor molecules collide with the cluster β_{het}, and the monomer concentration on the surface [42]. The heterogeneous Zeldovich factor is given by the Z_{hom} multiplied with a prefactor accounting for the shape of the seed particle [40]. Heterogeneous nucleation rate is hard to measure experimentally [43]. Commonly the nucleation probability P is used instead. P is dependent on the nucleation rate via the following equation [43]:

$$P = 1 - exp(-J_{het} \cdot t) \tag{2.21}$$

Eq.(2.21) describes the probability that nucleation takes place for one condensation nucleus within a time t [42]. The nucleation probability can also be expressed as the ratio between nucleated particles (or also activated particles) over the total particles [43]:

$$P = \frac{N_{act}}{N_{tot}} \tag{2.22}$$

Nucleation Theorem

The nucleation theorem is a general relation connecting thermodynamic variables, governing nucleation, to the nucleus size (nucleation work, respectively) [44]. In eq.(2.23) the relation between the nucleation rate and the supersaturation is given [45], [46]:

$$\left.\frac{\partial ln J}{\partial ln S}\right|_{T=const} = n^* + 1 \tag{2.23}$$

This relation gives n^* which is the number of molecules in the critical cluster that are in excess of the number of molecules in the vapor phase occupying the volume of the critical cluster [43]. Given the low number of molecules in the (small) volume of the critical cluster, the excess molecules can be approximated by the actual number of molecules in the critical cluster [43].

2.3 Charging Effect

When accounting for charges, the Kelvin equation, eq.(2.11), is extended to the so-called Kelvin-Thomson equation [43]:

$$ln S = \frac{2\sigma}{n_l\, k\, T\, r^*} - \frac{q^2}{32\pi\, \epsilon_0\, n_l\, k\, T\, r^{*4}} \cdot \left(1 - \frac{1}{\epsilon_l}\right) \tag{2.24}$$

The added term consists of the vacuum permittivity ϵ_0 , the relative permittivity of condensing liquid ϵ_l and the total electric charge q (= i·e). The latter is given by the number of charges i times the elementary charge e.

Figure 2.5 shows the impact of charging as a function of particle diameter. Comparing Kelvin, Kelvin-Thomson singly charged and Kelvin-Thomson doubly charged, it is clearly visible that the general charging state only plays a role for sub 5nm particles [43]. Only considering singly charged states, a significant influence is observed for even smaller particles. On the x-axis $\mathcal{D}_p$ is depicted, which is the geometric particle diameter.

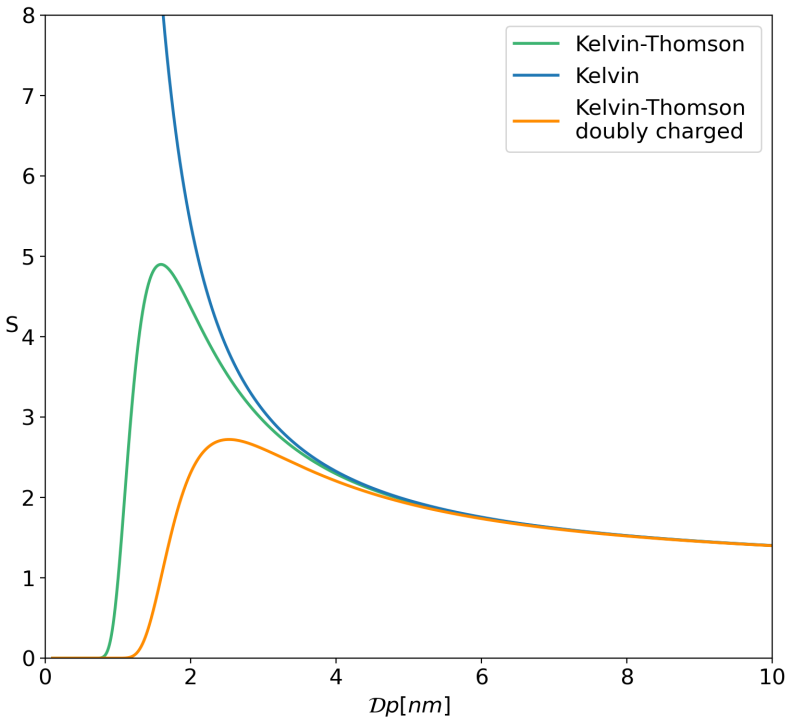

Figure 2.5: Theoretical calculation of the Kelvin curve eq.(2.11) and the Kelvin-Thomson eq.(2.24) curve for singly and doubly charging.

2.4 Physicochemical Properties

In the gas phase molecules move freely, overcoming attractive forces between them [47]. If the movement is less vigorous, intermolecular attractive forces become more significant bringing molecules closer together [47]. In the condensed phase (liquid or solid) they are packed tighter leading to a higher density [47]. In other words, the weak interaction between molecules is the reason for the existence of the condensed phase [48]. Intermolecular attractions result from electrostatically driven interactions between charges, permanent dipoles and induced dipoles. For deeper insight into the formation of liquids, we thus need to understand the electric properties of molecules [48].

Dipole moment, Polarity

Such an important property is the electrical dipole. An electrical dipole occurs when two opposite charges +q and -q are in a distance l [47]. The dipole moment is given as [48]:

$$d = q \cdot l \tag{2.25}$$

Even molecules with no net charge can have a charge separation and can be a polar molecule or a nonpolar molecule. The former is a molecule with a permanent dipole moment [47]. A permanent dipole only occurs in asymmetric molecules and therefore never in single atoms [49]. Unpolar molecules, on the other hand, do not have a permanent dipole but they can have an induced dipole moment due to an external field that has an influence on the electron distribution.

Electronegativity

The energy needed to withdraw an electron from an atom and therefore forming a positive ion and a free electron is called ionization energy [47]. Contrary, the electron affinity is the energy that is released when a free atom and a free electron are combined, forming a negative ion [47]. The chemical property of an atom to attract an electron is called electronegativity [47]. The electronegativity inversely correlates with the atomic radius. The atomic radius decreases (while the electronegativity increases) from left to right and increases (electronegativity decreases) from top to bottom within the periodic table [50].

Water consists of two hydrogen atoms (each with one electron in its outer shell) and one oxygen atom with 6 electrons. An illustration of a water molecule is given in Figure 2.6. Covalent bonds between these three atoms lead to the formation of one water molecule. The electrons from the hydrogen atoms are drawn to the oxygen atom (due to the higher electronegativity of the oxygen atom), leading to partial charge separation [51]. In conclusion, the partial charge of the oxygen is negative (marked by the red area in Figure 2.6) and both hydrogen atoms have a positive partial charge. Due to this charge separation the water molecule is polar.

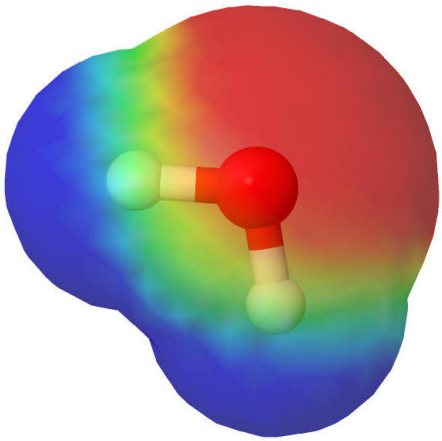

Figure 2.6: Illustration of a water molecule; Oxygen atom is colored in red and the two hydrogen atoms in white. The colored area around the water molecule indicates the polarity of the water since a charge separation between the one oxygen and the two hydrogen atoms is present. The red area indicates the negative partial charge and the blue area the positive partial charge; created with Jmol [52].

Polarizabilty

A molecule without charge separation is called nonpolar. However, for every atom and molecule a dipole moment can be induced [53]. An external electric field displaces the negatively charged electron cloud from the positive nucleus leading to the displacement of charges [53]. The magnitude of this induced dipole moment $\vec{d}$ divided by the strength of the applied electric field $\vec{E}$ is called the polarizability α [47]. This is a molecule specific parameter [47]:

$$\alpha = \frac{|\vec{d}|}{|\vec{E}|} \tag{2.26}$$

2.5 Intermolecular Forces

Forces between atoms and molecules vary due to their chemical and physical origins, strength, range and direction amongst others [54]. Common types of interactions will be introduced and briefly described in this chapter.

2.5.1 Covalent/Chemical Bonding

The formation of molecules are based on covalent bonds. They result from an overlap of atomic orbitals leading to a molecular orbital filled with two electrons obeying Pauli's principle [55]. Typically, both atoms provide one electron each. In multi-atom molecules the molecular geometry depends on the location or spatial distribution of the atomic orbitals (i.e. hybridization) resulting in well defined bond distances and bond angles [56]. In Figure 2.6 a water molecule is depicted consisting of one oxygen atom covalently bonded to two hydrogen

atoms. The remaining electrons from the oxygen that are not taking part in the covalent bonds are located in lone pairs [57].

2.5.2 Electrostatic Interactions

Electrostatic pair interactions describe the attractive or repulsive forces between charges. These interactions are long-range and therefore relevant for distances beyond the closest neighbouring atoms [58]. Herein, several possible cases will be discussed and a summarized list with corresponding energy values is given in Table 2.1 .

Charge - Charge

The strongest electrostatic interaction is between two charges, as specified in the Table 2.1. This interaction is based on the Coulomb force and is a long-range force. An ionic crystal such as NaCl, for example, is primarily formed due to the ionic forces between the sodium (Na^+) and chloride (Cl^-) ions [59].

Charge - Dipole and Dipole - Dipole

Atoms with different electronegativities usually form molecules with a distorted charge distribution, leading to a dipole moment within the molecule [60]. This dipole can be attracted by charges or other dipoles [60]. An example for the interaction between a charge and a dipole is the interaction between an ion and water. Compared to ionic bonds and charge-dipole interaction, the force between two polar molecules is less strong because the charge of a dipole is smaller than the charge of an ion [60].

A particular important interaction is the so-called hydrogen bond, formed between an electron depleted H atom and an electronegative atom. Figure 2.7 shows a scheme of a hydrogen bond. The bond (indicated by the dotted line) is formed between the lone pair of the electronegative oxygen atom from the right water molecule and the electron depleted H atom from the left water molecule. This hydrogen bond is unique because of its partial covalent character. [61]

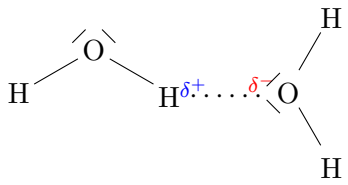

Figure 2.7: Hydrogen bond formed between an electron depleted hydrogen atom and an electronegative (oxygen) atom, shown by the example of two water molecules.

Charge - Induced Dipole and Dipole - Induced Dipole

Inductive interactions occur due to the fact that a charge or a permanent dipole generates an electric field which induces a dipole moment in a nonpolar molecule with polarizability α [60]. The strength of the electric field of a dipole is less than for an ion. Therefore the resulting force is weaker between the interaction of a dipole and the nonpolar molecule compared to the interaction between a charge and a nonpolar molecule. The strength, in general, depends on the polarzability of the nonpolar molecule, the strength of the dipole moment of the polar molecule or the charge of the ion, respectively [60].

Induced Dipole - Induced Dipole

For a nonpolar molecule the time-averaged dipole moment is zero [62]. However, fluctuation in the charge distribution leads to the formation of a dipole moment which in terms generates an electric field that polarizes any nearby atoms/molecules [62]. This interaction between two nonpolar molecules is called (London) dispersion interaction [60]. Van der Waals forces are an umbrella term for dispersion forces and the forces between dipole-dipole and induced dipole - dipole forces.

The table below shows the above mentioned interactions with their average magnitudes and distance dependencies respectively. This list should serve as an estimate and reference.

Interaction	Energy	Distance	Example
charge-charge	-20 to -40kJ/mol	$1/r$	$Na^+ + Cl^-$
charge-dipole	-12 to -20 kJ/mol	$1/r^2$	$Na^+ + H_2O$
dipole-dipole	-4 to -12 kJ/mol	$1/r^3$	HCl + HCl
charge-induced dipole	-2 to -10 kJ/mol	$1/r^4$	$Fe^{2+} + O_2$
dipole-induced dipole	-2 kJ/mol	$1/r^6$	H_2O + Xe
hydrogen bonds	-4 to -30kJ/mol		$H_2O + H_2O$
dispersion	-2 to -4 kJ/mol	$1/r^6$	O_2

Table 2.1: List of different non-covalent interactions with their typical energies and distance dependencies, adapted and modified from [60].

3 | Material and Methods

In this section the instruments used in this study will be introduced and their working principles explained, together with the experimental setup and the (day-to-day) workflow.

3.1 Supersaturation

The establishment of supersaturated vapor is important in several steps within the experimental setup. In general, there are three ways how supersaturation can be achieved : temperature gradient, adiabatic expansion or turbulent mixing [43]. The details will be given in the specific sections.

3.2 Particle Generation

Stable conditions are crucial for quantitative measurements. The production of particles at a constant concentration is of great importance. Herein, nano-sized particles are produced by evaporating the material in question followed by vapor nucleation [31]. The formation is based on homogeneous nucleation [31]. The necessary supersaturation for this process is achieved by a temperature drop. The material in question is inserted using a glass crucible into a tube furnace where it is evaporated. This method of particle generation was shown to deliver constant concentrations over a large time span [31].

3.2.1 Plastics, Sodium Chloride and Silver

By definition plastic is a polymeric material [18]. Polymeres describe a class of macromolecules that consists of n repeating monomeres [63]. This thesis will focus on Polyethylene terephthalate (PET). The chemical formula of PET is $[C_{10}H_8O_4]_n$ [64]. The molecular structure is shown in Figure 3.1. It consists of alternating moieties of nonpolar (benzene ring) and polar (ester functionality) groups. Two different forms of PET were analyzed: pellets (pPET) and snippets of a transparent plastic water bottle (cPET). In the following the prefix **p** anc **c** is used to distinguish between the chemical standard ("**p**urity") version and the **c**ommodity version of PET.

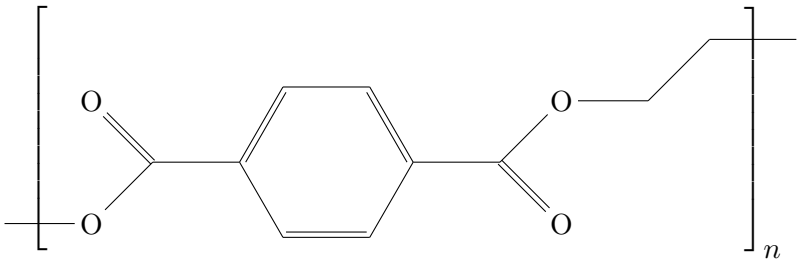

Figure 3.1: Structural formula of Polyethylene terephthalate (PET) with the chemical formula $[C_{10}H_8O_4]_n$. [65]

Sodium chloride (NaCl) was used as a calibration and reference material in the following measurements. Another reference material was silver (Ag). A table of the technical information including the CAS numbers and the melting points of the material in use is given in the Appendix (Table 8.1).

3.2.2 Tube Furnace

A schematic description of a tube furnace is given in Figure 3.2. It consists of a cylindrical hull with heating walls with an embedded ceramic tube inside. To ensure an enclosed system a glass tube is mounted additionally inside the ceramic tube. The material of interest can be inserted using a glass crucible. In order to maximize consistency in heat transfer during the measurements, the glass crucible was inserted each time in the middle of the tube furnace. Once the oven is heated up at a high enough temperature, depending on the material properties, the material of interest will evaporate. A carrier gas transports the evaporated material to cooler regions. This temperature drop leads to a supersaturation and due to homogeneous nucleation aerosol particles are formed. The glass used for the crucible and the tube inside the furnace is quartz glass. This material is resistant to higher temperatures and ensures that no unintended particles coming from the glass are generated within the process.

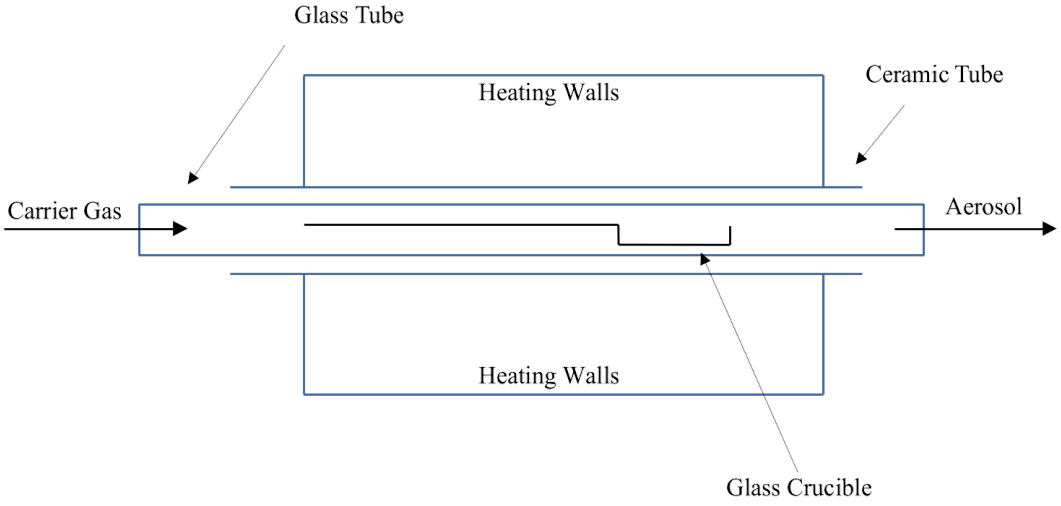

Figure 3.2: Schematic drawing of the tube furnace in use, based on [66]

Two different tube furnaces were used. As heating element for the generation of plastic nano-particles the Nabertherm tube furnace R50/250/13 was used. For the generation of salt and silver nano-particles a custom-build tube furnace was used [67]. This way, nano-particles were generated in the same manner as the comparative studies.

3.3 Size Classification by Differential Mobility Particle Sizer

The differential mobility particle sizer (DMPS) for these measurements consists of an aerosol charger (charging the particles), a differential mobility analyzer DMA (selection of a specific mobility) and a particle counter.

3.3.1 Aerosol Charging

As aerosol charger the TSI Advanced Aerosol Neutralizer 3088 was used. Herein, soft x-rays produce ions of positive and negative charges which will then charge the aerosol particles due to random collisions (Bipolar diffusion charging) [68].

A mathematical description of the charge distribution for aerosol particles in a bipolar atmosphere is given by Fuchs' theory [69]. Based on this model, Wiedensohler introduced an approximate formula, see eq.(3.1), which describes the charging probability for a particle at size dp with charging state N [70]. a_i(N) are approximation coefficients [70]. As stated by the author, this approximation is only valid for $0 < \mathrm{dp} < 1000\mathrm{nm}$ and for $-2 < \mathrm{N} < 2$ [70].

$$f_c = 10^{\left[\sum_{i=0}^{5} a_i(N)\cdot\log(dp/nm)\right]} \tag{3.1}$$

In Figure 3.3 the charge distribution function is plotted against the particle diameter for neutral particles, singly charged particles (positive and negative) and doubly charged particles (positive and negative). The plot shows that for sizes larger than 4nm, respectively 5nm, a small proportion of particles gets negatively respectively positively singly charged. With increasing particle size, the probability that particles get singly charged increases and following the probability of particles with no charge (N=0) decreases.

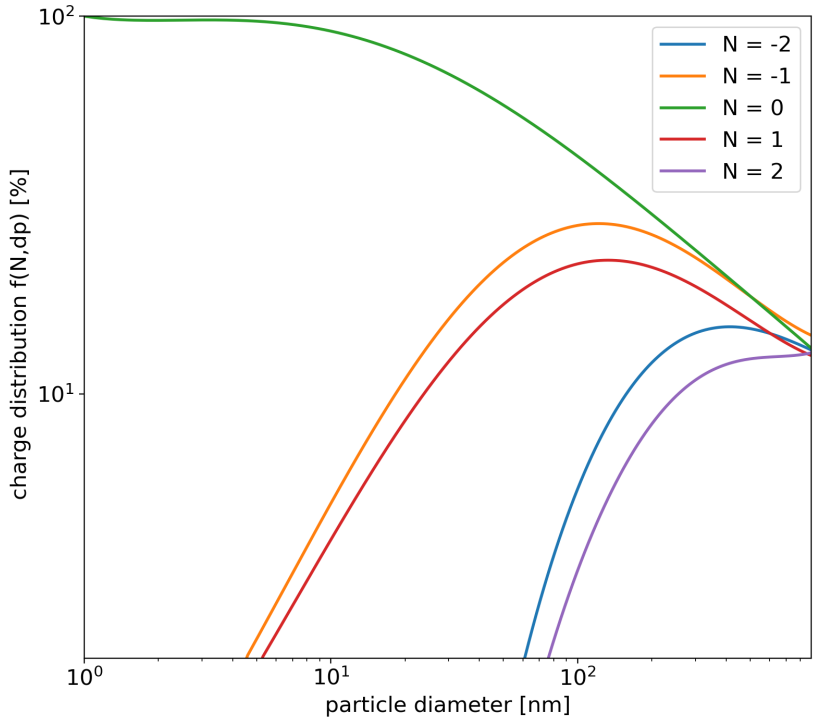

Figure 3.3: Charging probability f_c versus diameter dp for 5 different charging states N

The need to account for the effects of double charging is only relevant for particle sizes bigger than 60nm, as can be seen from Figure 3.3. For these experiments the highest particle size was about 11 nm and the charging state was -1. Therefore double charging was of no concern.

3.3.2 Differential Mobility Analyzer

Mono-dispersed aerosols were required for the conducted experiments. For size selection a Vienna-type differential mobility analyzer (DMA) was used. In Figure 3.4 a schematic setup is depicted. The Vienna-type DMA is a cylindrical capacitor with radius R_2 and length L with a central rod (R_1) and a narrow exiting slit. An electric field is generated by the applied voltage HV. The sign of the voltage determines if negative or positive particles are selected. When charged aerosol particles (Q_A) enter the DMA they are dragged along with the sheath

flow (Q_{sh}) through the DMA. The electric field deflects the aerosol particles and only those with specific mobility Z will pass through the exiting slit, resulting in the separation of the sample flow (Q_S) with particles of desired mobility and the excess flow (Q_{ex}). In general, the mobility Z of a spherical particle with diameter dp is given by eq.(3.2). This mobility depends on the slip correction factor C_c, elementary charge e, the number of charges i carried by the particle and on the viscosity of the carrier gas η, herein the viscosity of air. [71]

$$Z = \frac{ie}{3\pi\eta} \cdot \frac{C_c(dp)}{dp} \tag{3.2}$$

The Cunningham slip correction factor accounts for the case when the particle size becomes comparable to the mean free path λ of the carrier gas [71] and is given by the following equation [72]:

$$C_c(dp) = 1 + 2.492 \cdot \frac{\lambda}{dp} + 0.84 \cdot \frac{\lambda}{dp} \cdot exp\left(-0.43 \cdot \frac{dp}{\lambda} \right) \tag{3.3}$$

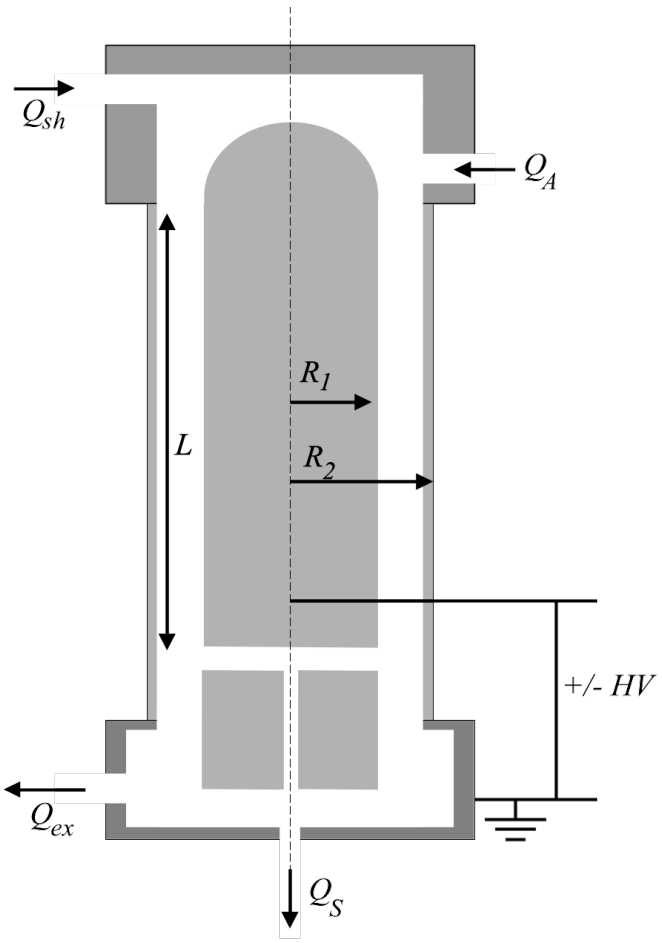

Figure 3.4: Schematic drawing of a Vienna type DMA based on [72]; aerosol particles enter (Q_A) and are dragged with the sheath flow (Q_{sh}) through the DMA. An applied voltage (HV) deflects charged particles and only those with specific mobility pass through the exiting slit (Q_S). The remaining particles are exiting with the excess flow (Q_{ex}). [72]

The mobility of a particle moving inside the Vienna type DMA is a function of the applied voltage V, the DMA's geometry and the flow rates (Q) [71]:

$$Z = \frac{1}{V} \cdot \frac{ln(\frac{R_2}{R_1})}{2\pi L} \cdot \frac{(Q_{sh} + Q_{ex})}{2} \tag{3.4}$$

The resolution β of the DMA is given by the sum of the aerosol and sample flow, divided by the sum of the sheath and excess flow [73]:

$$\beta = \frac{Q_a + Q_s}{Q_{sh} + Q_{ex}} \tag{3.5}$$

Eq.(3.2) and eq.(3.4) leads to a formalism, eq.(3.6), that connects the applied voltage to the particle diameter. This diameter is the so-called mobility equivalent diameter dp.

$$V = \frac{ln(\frac{R_2}{R_1})}{2\pi L} \cdot \frac{(Q_{sh} + Q_{ex})}{2} \cdot \frac{d_p}{C_c(d_p)} \cdot \frac{3\pi\eta}{ie} \tag{3.6}$$

The DMA can be operated in two different modes [71]. For selecting a mobility diameter, a specific voltage value is applied. Due to the dependence of the cunningham factor eq. (3.3) on the particle diameter, the data needs to be inverted to calculate the diameter from the applied voltage. In this mode a mono-dispersed aerosol is generated. In the scanning mode the voltage varies and gives the concentration for different mobility diameters. This results in a particle number size distribution (PNSD). The applied voltage ranges from 0V to 10000V (sectioned into 97 channels), resulting in an upper limit of about 40nm in the present setup.

3.4 Particle Counters

Concentration measurements were performed using two different particle counters relying on different working principles. In the following, these two different techniques will be explained in more detail.

3.4.1 Condensation Particle Counter

A condensation particle counter (CPC) is used for detecting ultra-fine particles [74]. Basically, it consists of a saturator, condenser and an optical element. According to [75] the physical principal of this instrument is heterogeneous nucleation. Due to the temperature difference between the saturator and the condenser the working fluid becomes supersaturated. Nucleation on the aerosol particles is initiated followed by condensational growth. Hence, the particles become large enough to be detected by an optical element. The particle counter used in the set up was the Ultrafine Condensation Particle Counter (UCPC) Model 3776 from TSI [75]. A schematic representation of the CPC is given in Figure 3.5. Air is pumped continuously through an inlet. This inlet flow can be operated in two different modes: low-flow (0.3lpm)

and high-flow (1.5lpm). The working fluid of the CPC in use was n-butanol. A wick soaked with the working fluid is heated in the saturator at 39°C. Vaporized butanol is mixed with the aerosol sample and enters the condenser which is cooled at 10°C. Due to the temperature gradient the gas condenses and grows on the particles. Subsequently, the particles enter the optical element (heated at 40°C) and are counted. This temperature setting is simply to avoid vapor condensation on the optical elements. The great advantage of the CPC is the ability to count single particles. [75]

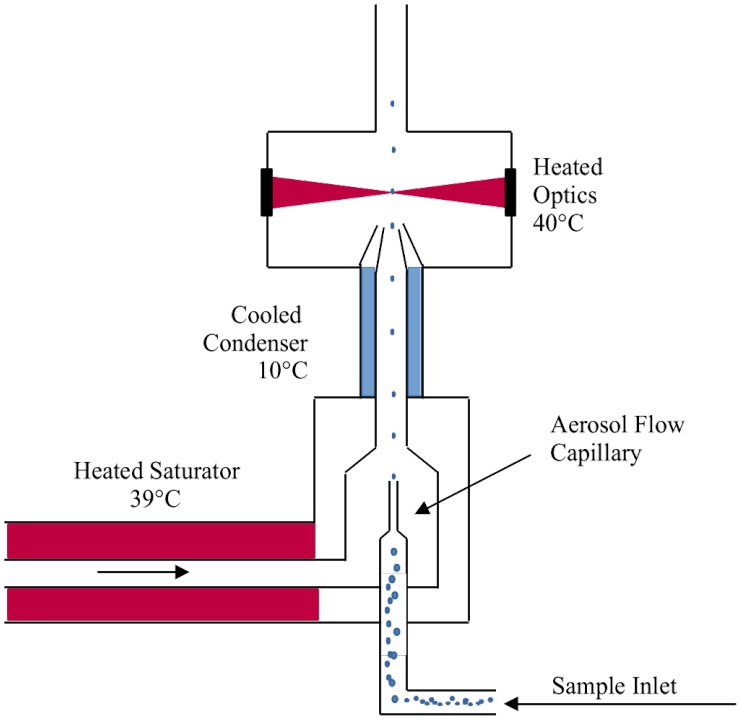

Figure 3.5: Schematic drawing of the model 3776 UCPC based on [75].

To avoid homogeneous nucleation, the temperatures of the saturator, the cooler and the optical element are controlled. This is necessary because the CPC needs to operate below the supersaturation value that would initiate homogeneous nucleation [76]. Due to the limited S applied a decrease in particle size usually reflects in a rapid drop of detection efficiency. The 50 % cutoff is a concept of describing the detection efficiency of CPCs [76]. This value gives the particle size at which 50 % are activated by heterogeneous nucleation and can therefore grow to detectable sizes. This detection limit of the UCPC 3776 is given as 2.5nm according to the manual [75]. However, based on the paper of Wlasits et al. (2020) the cutoff is not only depending on the working fluid but also on the particles characteristic - or more explicitly, the chemical interaction between the working fluid and the particle material [76]. In a nutshell, chemical similarities between the working fluid and the seed particles have an impact on the detection efficiency [76]. Therefore the cutoff given as detection efficiency by the manufacturers can not be taken completely for granted. For instance, the 50 % cutoff for NaCl particles with the UCPC Model 3776 was found to be at 4,0 ± 0.1 nm [76].

3.4.2 Faraday Cup Electrometer

An alternative method for the size-independent detection of nano-sized and electrically charged aerosol particles is based on the principle of a faraday cage. A schematic setup of the so-called Faraday Cup Electrometer (FCE) is depicted in Figure 3.6. An external pump draws a charged aerosol sample with flow rate q_e inside the FCE. An insulated filter collects the charged particles leading to an electric current, subsequently measured by a highly sensitive amperemeter. [77]

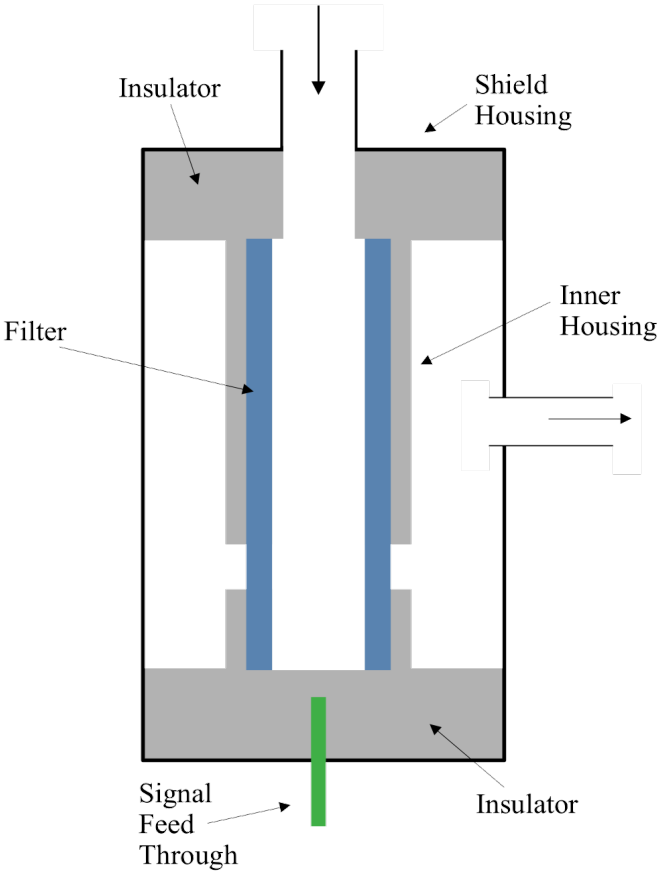

Figure 3.6: Schematic drawing of an Aerosol Electrometer Model 3068, based on [78].

From the resulting current I_e , the particle number concentration N can be calculated using eq.(3.7) [78]. The elementary charge is denoted by e, q_e is the flow rate and n_p is the number of charges per particle. However, for the performed measurements multiple charging can be neglected, as shown in Figure 3.3. For the measurements the Aerosol Electrometer Model 3068 from TSI [78] was used.

$$N = \frac{I_e}{e \cdot n_p \cdot q_e} \tag{3.7}$$

According to the manufacturer, the FCE is able to measure particles as small as 2nm [78]. The FCE has the advantage that, it does not have a cut-off, unlike the CPC. However,

because of external disturbances this instrument has a background signal. This offset needs to be subtracted from the signal. So the FCE has the advantage to resolve smallest particle sizes, but has an offset which influences its efficiency especially for low concentration. The CPC for comparison has a cutoff which is dependent on working fluid and the particle size, but is a very sensitive instrument for low concentration measurements. So even a single particle can be detected.

3.5 Size Analyzing Nuclei Counter

The Size Analyzing Nuclei Counter (SANC) is an expansion type CPC that was developed at the University of Vienna and gives the unique opportunity to study heterogeneous nucleation at well-defined saturation ratios [79]. Due to an adiabatic expansion, accomplished by a pressure drop over a few ms, supersaturation is achieved and droplets grow in the expansion chamber and are subsequently illuminated by a laser [43], [80],[81]. In Figure 3.7 an illustration of the optical element of the SANC is depicted.

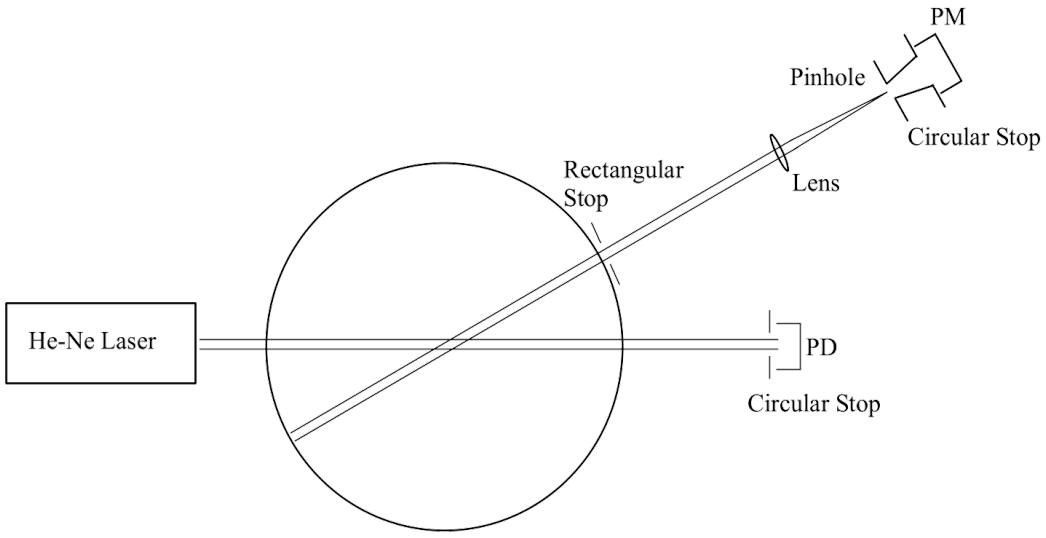

Figure 3.7: Schematic of the optics of the SANC, PD photodetector, PM photomultiplier, based on [80].

A helium neon laser is mounted with a wavelength of 632,8nm [82]. The transmitted light is measured by a photo-detector (PD). Scattered light fluxes are focused by a lens to a photo-multiplier (PM) at an angle of 15° [80]. Since particle sizes become as large as the wavelength of the laser, the scattering regime follows Mie theory ($\lambda \sim$ dp). By comparing experimental scattering intensities to theoretical scattering spectra, droplet size and concentration can be calculated according to the Constant Angle Mie Scattering CAMS method [81]. Figure 3.8 shows exemplary theoretical and experimental scattering spectra.

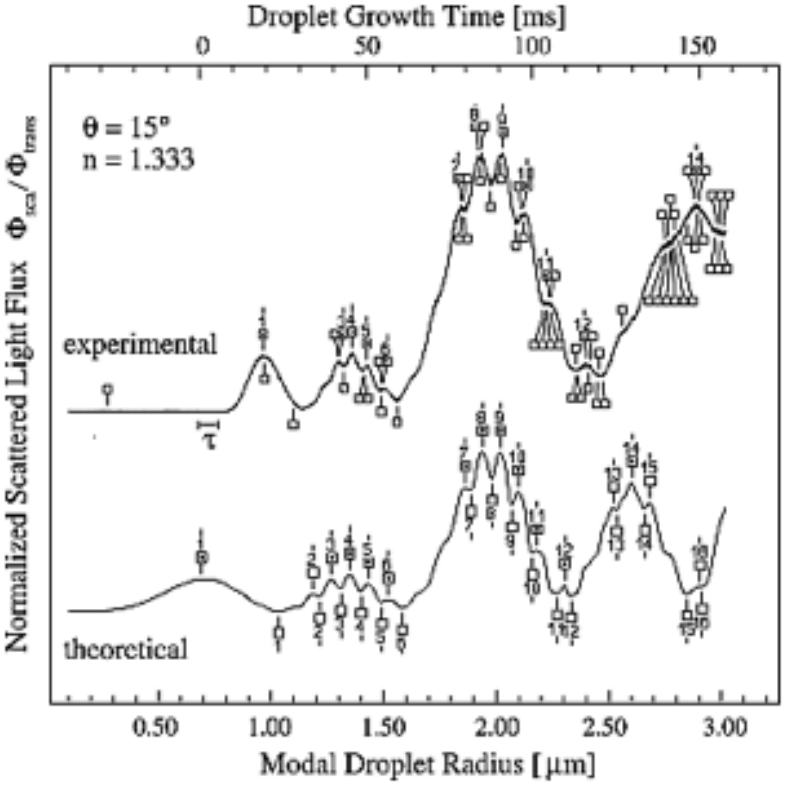

Figure 3.8: Experimental and theoretical Mie sepctra for an angle of 15°, by identifying the extrema particle concentration and particle size are calculated using Mie theory [80].

Measurements are controlled by the program ACQUIRE, which was developed by W. Szymanski and controls a series of measurement cycles. This cycle or also called "shots" is a sequence of several steps. They differ from opening or closing magnetic valves remotely via an electronic valve control unit. A schematic description of these valves is given in Figure 3.9. The sequence of one cycle is as follows: [39]

- **Flushing:** Valves V6, V3 and V1 are open. Aerosol sample and filtered/dried air is flushing through the expansion chamber.
- **Delay:** V4 is opened and V3 is closed, ensuring continuous aerosol flow and letting the aerosol equilibrate with the chamber thermal conditions .
- **Expansion:** V6 is closed and V2 is opened, connecting the expansion chamber (EXP) to the sub-pressure vessel (R)
- **Pressure adjustment:** V6 is opened and to balance the expansion chamber that is under-pressure with the surrounding ambient air pressure V5 is opened.

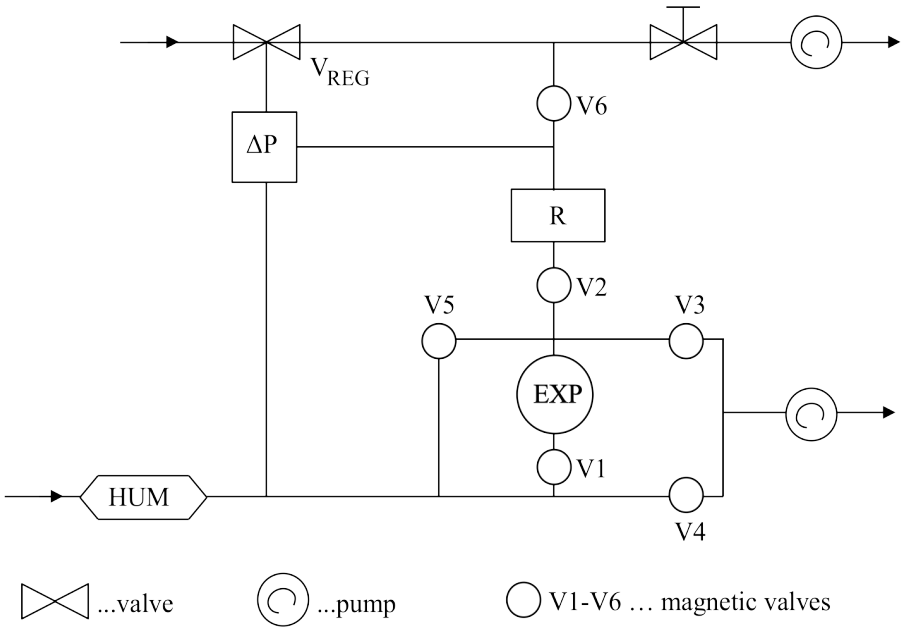

Figure 3.9: Schematic setup of the SANC, modified from the original electronic valve control unit.

After the pressure adjustment the cycle starts again by flushing carrier gas and the aerosol through the expansion chamber [39]. The times for flushing and delay can be set and are computer controlled. For the performed measurements these times are given in the Table 8.4, which can be found in the Appendix.

Before starting a measurement, (ambient) conditions need to be fed into the ACQUIRE software, i.e. ambient air pressure, temperature of the humidifier (T_{Hum}), relative humidity (RH) inside the humidifier, particle radius (r) of the aerosol particles and temperature of the chamber (T_{Cha}). The pressure drop inside the expansion chamber happens adiabatically (without the transfer of heat) [46]. This is achieved by a short expansion time (a few ms). After passing through the humidifier the aerosol enters the expansion chamber with an initial temperature T_i. The pressure inside the chamber before expansion is p_i and is equal to the atmospheric pressure. The pressure drop can be described by the expansion ratio β and is given as [82]:

$$\beta = \frac{p_i}{p_0} = \frac{p_i}{p_i - \Delta p} \tag{3.8}$$

The partial vapor pressure after the expansion is dependent on the expansion ratio, the relative humidity and the saturation vapor pressure [82]:

$$p_v = \frac{RH \cdot p_s(T_{hum})}{\beta} \tag{3.9}$$

The temperature T_2 after the expansion is not measured but calculated using eq.(3.10) , where κ is the adiabatic coefficient [82]:

$$T_2 = \frac{T_i}{\beta}^{\frac{\kappa-1}{\kappa}} \tag{3.10}$$

Ultimately, the saturation ratio S after the expansion can be calculated from the ratio of the partial vapor pressure p_v, eq(3.9), and the saturation vapor pressure p_s at temperature T_2 :

$$S = \frac{p_v}{p_s(T_2)} \tag{3.11}$$

Scattering curves for each pressure value were measured five times (so-called 'shots') and are given as averages. Changing the pressure of the sub-pressure vessel, the saturation ratio after the expansion can be varied. With increasing S, gradually more particles will nucleate until a plateau is reached where all particles inside the chamber have nucleated (also called activated). The nucleation probability P(S) can be calculated by taking the ratio of the concentration divided by the total concentration eq.(2.21) [43]. The function P(S), the so-called activation curve, resembles a sigmoid function. A comparison between different activation curves was performed by investigating the onset saturation ratios S_0 of each curve. This value is defined as the saturation ratio where 50 % of the particles are activated.

$$P(S_{onset}) = P(S_0) = 0.5$$

The temperature at this saturation ratio is given as the nucleation temperature T_0.

3.6 Experimental Setup

Before going into detail about the specifics of the performed experiments it should be mentioned that the measurements for this master thesis were performed in close collaboration with Peter Wlastis. In the wake of this thesis, the paper with the title "Heterogeneous Nucleation of Supersaturated Water Vapor onto Sub-10 nm Nanoplastic Particles" [67] was published.

An illustrative description of the setup is given in Figure 3.10. The setup can be divided into three different parts: particle generation, DMPS and SANC. First of all, the test aerosol needed to be generated. Therefore, the material in question was heated up in the tube furnace and carried by dried and filter air (Q_f) to a water-jacketed condenser, where aerosol particles were formed due to homogeneous nucleation. The temperature of the water inside the condenser was controlled by a RM6 Lauda circulating water bath chiller [83]. Dried and filtered air ($Q_{dil,1}$) dilute the aerosol samples. This is necessary since a minimum flow rate is needed in the setup. The CPC was operated with a flow rate of 1.6lpm and the SANC also with a flow rate of 1.6lpm. Higher flow rates in the tube furnace have an affect on the production of

nano-sized particles. Therefore the flow was divided into dilution and furnace flow. Entering the DMPS, the aerosol got charged and the DMA selected a mobility equivalent diameter, according to the applied voltage. If the particle concentration was too high, a second dilution ($Q_{dil,2}$), again of dried and filtered air, was mounted right after the DMA. Splitting the flow, one part is going to the CPC (for monitoring stability of particle concentration), whereas the other part enters the humidifier. The humidifier consists of a water-jacketed cylindrical tube with a humid wick inside. By controlling the temperature of the surrounding water with the circulating water bath chiller Lauda RK20 [84], the relative humidity was controlled. High flow rates (above 2 lpm) have an effect on the RH inside the humidifier. Consequently, right before the entrance to the SANC an RH sensor was mounted for monitoring reasons. The temperature of the chamber inside the SANC was controlled via a circulatory cooling unit (Lauda VC1200 Vario Cool [85]).

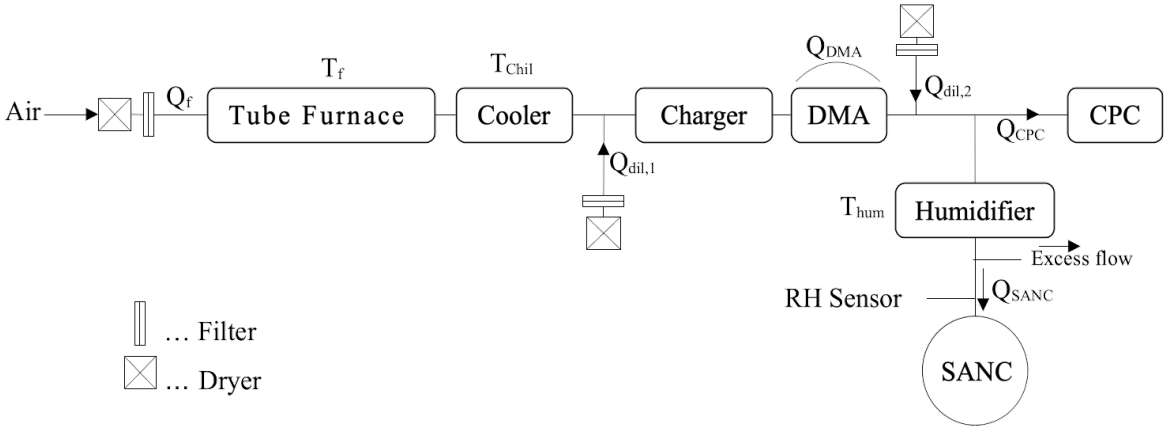

Figure 3.10: Schematic of the experimental setup; Q indicates the various flow rates.

As Figure 3.10 shows, the CPC is mentioned as particle counter. The FCE was also tried in the attempt to achieve smaller particle sizes. Overall, there was no benefit in switching to the FCE. Therefore, the CPC was mainly used to measure the concentration. The particles that were selected and fed into the SANC were negatively charged due to the positive voltage applied to the DMA. The activation of neutral particles was also observed. For this measurement the setup needed to be slightly changed. After the DMA and before entering the humidifier a second aerosol charger was mounted as well as an ion trap. The changed setup is shown in Figure 3.11.

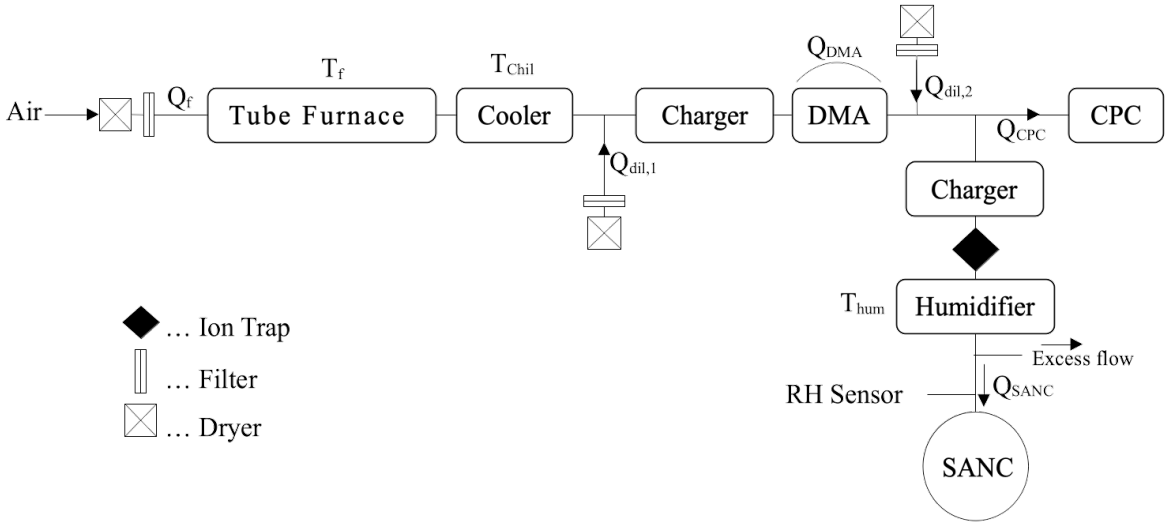

Figure 3.11: Modified setup, including a second charger and an ion trap to generate neutral sample particles.

3.7 Experimental Workflow

In this section, the day to day workflow will be discussed. Listed above are the necessary steps for measuring:

1. waiting for the cooler following the furnace to reach a temperature of $T_{Chill} = 10°C$
2. checking humidity of the flows
3. checking and adjusting flow rates
4. heating up the furnace and background measurement of the tube
5. inserting the crucible with the material of interest and waiting for around 30 minutes to ensure a stable particle generation
6. PNSD measurement
7. selection of the mobility equivalent diameter
8. checking the wick in the humidifier, eventually wet with H_20
9. adjusting the temperature of the humidifier
10. starting SANC and connecting to setup, waiting for the stabilization of the RH inside the humidifier
11. setting the conditions needed for the SANC (T_{hum}, T_{Cha}, P, r,..)
12. starting SANC measurement using the program ACQUIRE

13. evaluating the data using the program REDUCE

14. comparing the theoretical growth to the experimental growth rates

15. data extraction from SANC

The daily workflow can be divided into two steps. Firstly, sample particles were generated and selected via their mobility diameter. Secondly, the SANC and the humidifier were prepared. Crucial for the performance of the experiments is the establishment of thermodynamic equilibrium. Therefore waiting periods were necessary. Especially challenging was the achievement of an equilibrium of the RH inside the humidifier. The RH was not only influenced by changes from external conditions (e.g. ambient pressure or temperature) but also from variations concerning the flow rates passing through the humidifier.

First of all, while the cooler reaches 10°C **(Step 1.)** flow rates were measured and their humidity was checked **(Step 2.+ 3.)**. If the RH was above 10% the silica gel of the dryers was changed. The tube furnace was heated up and after reaching its temperature a background measurement was performed to ensure that no artefacts influence the measurements **(Step 4.)**. Herein, the DMA was used in scanning mode and the concentration was measured. During this process, for the whole diameter range no particles should be detected. After this step, the glass crucible with the material was inserted **(Step 5.)** and a waiting period of 30 minutes has empirically shown to reveal stable particle concentrations. After this step, a PNSD was recorded, if desired **(Step 6.)**. Changing the voltage of the DMA the desired mobility diameter was selected **(Step 7.)** and the concentration was checked. Eventually, $Q_{dil,2}$ had to be adjusted accordingly to achieve a specific concentration range. Empirically, a concentration between 10 000 - 30 000 /cm^3 delivered good spectral images which was important for evaluating the data afterwards [67]. Especially for smaller sizes the flow rates of the furnace and the dilution needed to be varied to achieve enough particle concentration. Afterwards, the SANC was prepared for the measurements. The wick in the humidifier was checked **(Step 8.)**, and if necessary water (HPLC grade water, see Appendix Table 8.1) was added. Periodically, the wick was exchanged to avoid any form of moldiness. After adjusting the temperature in the humidifier **(Step 9.)** the SANC was connected to the particle generation **(Step 10.)**. Again, a waiting period was necessary until the humidifier reached a stable RH. In order for the program to correctly calculate the saturation ratio inside the chamber ambient conditions and several other values (see Table 3.1) are needed to be passed to the SANC **(Step 11.)**. For the whole measurement the concentration as well as the RH was measured for monitoring reasons. Fluctuations in the concentrations and in RH values are unavoidable. However, if the concentration or the RH respectively, changed significantly the measurement was aborted. After finishing the experimental part of the measurements,

the acquired data were analyzed **(Step 13.)**. At the end of the day several data sets were acquired. A list of the file names and description is given in the Appendix (Table 8.5). A detailed description on the data acquisition using the SANC is given within the next Chapter (Chapter 4.2).

acronym	**description**
P	ambient pressure
T	ambient temperature
T_{hum}	temperature of the humidifier
T_{cham}	temperature of the expansion chamber
r_{init}	initial radius of the seed particle
RH_{set}	relative humidity

Table 3.1: Input variables for the ACQUIRE software that needed to be adjusted for each measurement (day).

4 | Data Evaluation

4.1 Particle Number Size Distribution

The particle number size distribution (PNSD) of the form of dN/dlog(d_p) is commonly used to describe aerosol size distributions [86]. To determine this value the concentration was measured using the CPC. However, to retrieve the raw size distribution it is necessary to account for losses due to the efficiency and resolution of the instruments. A scheme for this conversion, is given in Figure 4.1. The charge probability function is given by f_c which was introduced in the Chapter 2.3 where the charge probability depending on the size and charging state was discussed. The transfer function Ω of the DMA is given as the probability that a particle passes successfully through the instrument [87]. η_{CPC} is the counting efficiency of the CPC in use.

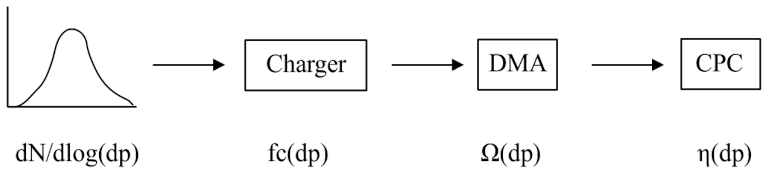

Figure 4.1: Illustrative description of retrieving a PNSD in form of dN/dlog(dp), altered from [88].

For a symmetric sheath and exhaust flow and symmetric inlet and sample flow as well as an assumed counting efficiency of the CPC ($\eta_{CPC} = 1$) the recovered size distribution can be calculated as follows where conc is the measured concentration by the CPC and β is the resolution of the DMA as introduced in eq.(3.5) [88]:

$$\frac{dN}{d\log d_p} = \frac{conc(d_p)}{\beta \cdot f_c}$$

Fit Functions

The analysis of different PNSDs was done by comparing the maximum values as well as the width of the distributions. Herein, the data was fitted using two different functions, a lognormal function eq.(4.1), or a skewed type-normal function eq.(4.2), which adds a skewness γ. $\hat{A}$ is the amplitude, σ the standard deviation, μ the mean value [86]. The parameters (maximum value and FWHM) that were taken to compare the different distribution were calculated from the retrieved functions.

$$f(x, \hat{A}, \mu, \sigma) = \frac{\hat{A}}{\sqrt{2\pi\sigma^2}} \cdot exp\Big(- \frac{(log(x) - log(\mu))^2}{2\sigma^2} \Big) \tag{4.1}$$

$$f(x, \hat{A}, \mu, \sigma, \gamma) = \frac{\hat{A}}{\sqrt{2\pi\sigma^2}} \cdot exp\Big(- \frac{(x-\mu)^2}{2\sigma^2} \Big) \cdot \Big(1 + erf\Big(\frac{\gamma(x-\mu)}{\sigma\sqrt{2}} \Big) \Big) \tag{4.2}$$

4.2 Size Analyzing Nuclei Counter

The SANC also provides a DATA Reduction Software (REDUCE). After measuring, the REDUCE program is called. This software enables the evaluation of the measured Mie spectra. With the function LOCATE experimental extrema in scattering curves are allocated to theoretical extrema. An example of this allocation is depicted in the Appendix (Figure 3.8). The CAMS method allows to calculate the size and the concentration of the particles inside the expansion chamber. In addition, the REDUCE program provides the calculation of theoretical growth rates, which gives the increase in droplet size as a function of time.

4.2.1 Activation Curve

Nucleation probability P(S) is a quantity that is most often compared in heterogeneous nucleation experiments [8]. This probability is calculated by taking the concentration for each saturation ratio S divided by the total concentration. The function P(S) resembles a step-function [8]. In the further analysis the onset saturation ratio S_0 was compared for various measurements. S_0 is the saturation value where half of the particles are activated, $S_0 = S(0.5)$. The Gumbel function, eq.(4.3), is used for fitting the activation curves. This probability distribution function is derived on basis of the nucleation theory [89] :

$$P(S) = 1 - exp\big(- exp\big[ln(ln2) + (n^* + 1) \cdot ln(S/S_0) \big] \big) \tag{4.3}$$

In a good approximation, n^* is given as the number of molecules in the critical cluster [43]. The slope of this activation curve at the onset saturation ratio is given as [89]:

$$\left. \frac{dP(S)}{dS} \right|_{S=S_0} = \frac{ln2}{2} \cdot \frac{(n^* + 1)}{S_0} \tag{4.4}$$

4.2.2 Growth

In addition to the calculation of the concentration using the CAMS method, the SANC provides its own analytical tool. Within the REDUCE program theoretical growth curves can be calculated and compared to experimental results. After evaluating an activation curve, the theoretical growth was compared to the experimental data. Herein, the growth was calculated in REDUCE using the command CALCULATE GROWTH. The results of this calculation were shown with PLOT GROWTH where a comparison to the experimental value was visible. If slight discrepancies between these two were observed, an error X on the saturation ratio S using MODIFY GROWTH_CALCULATION \SUPERSATURATION \ERROR X of the theoretical curve was applied to approach the experimental curve. An exemplary plot is shown in Figure 4.2. In panel (a) a good agreement between theoretical and experimental data is found. In contrast, in panel (b) the theoretical curve seems too steep to match the experimental data points. Including an \ERROR of -3% on the saturation for the calculation of the theoretical growth results in a better agreement with the data. It should be emphasized that it was not intended to determine or correct the onset saturation ratio values. This analysis was performed in order to avoid underestimated errors. In the case that the deviation between theoretical and experimental growth rate was bigger than the calculated one from gaussian error propagation (see next chapter) the deviation was incorporated into the error bars. Since this analysis suggests that the saturation ratio is bigger or smaller than theory would suggest, the approximated deviation was only considered in one way, which leads to asymmetrical error bars in the results below.

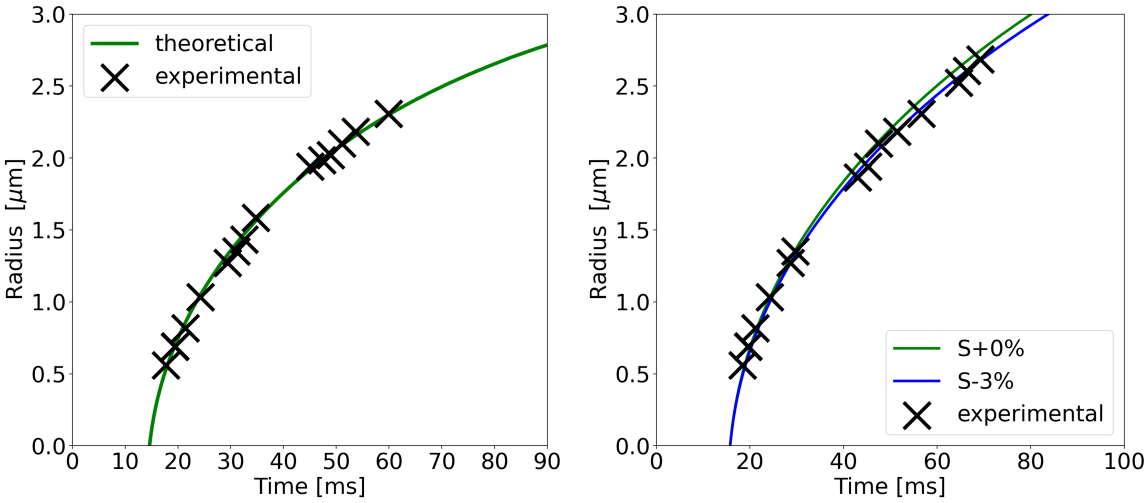

(a) Growth is calculated without a deviation of S.

(b) Growth is calculated with a changed saturation ratio of -3%.

Figure 4.2: Comparison between theoretical growth to experimental data, without and with a deviation of the saturation ratio.

4.3 Error Analysis

Particle Number Size Distribution

The error on the diameter originates from the resolution of the DMA given in eq.(3.5) and the error on the concentration is dependent on the instrument specifics of the CPC with ± 10% [75].

Size Analyzing Nuclei Counter

Performing the measurements, stable conditions were crucial. Therefore the concentration of seed particles and the RH inside the humidifier were carefully observed. Small fluctuations in these parameters are expected because a perfect thermodynamic equilibrium and conditions respectively can not be guaranteed. A threshold for these measurements was applied to minimize the effects of unstable conditions. If serious deviations were observed the measurements were aborted. In such cases, the concentration or the RH respectively, would exceed the specific error limits. This approach allowed beforehand to minimize errors. A statistical analysis was nevertheless performed. Herein the mean and standard deviation of the concentration were calculated. In the same manner, the evolution of the RH was analyzed with the addition that at the beginning of each measurement a RH value had to be set. Herein, the deviation in terms of the set value was calculated.

As explained in Chapter 3.5, in these experiments studying nucleation, supersaturation is achieved by adiabatic (fast, few ms) expansion. Vapor at specific temperature enters the expansion chamber and a fast pressure drop leads to supersaturation. In general, S is given as the ratio of partial vapor pressure p_v to saturation equilibrium vapor pressure p_s [37]. The latter is dependent on the temperature and can be calculated using eq. (4.5) [36]:

$$p_s(T) = exp\left(A_1 - \frac{A_2}{T - A_3} - A_4 \cdot ln(T) + A_5 \cdot T\right) \tag{4.5}$$

The coefficients are depending on the specific vapor in use. The values for water can be found in the Appendix. The partial vapor pressure p_v after the expansion is dependent on the expansion ratio β, RH and the saturation equilibrium pressure at the temperature of the humidifier [82]:

$$p_v = \frac{RH \cdot p_s(T_{hum})}{\beta} \tag{4.6}$$

The error on the supersaturation ratio S, eq.(3.11), was estimated by gaussian error propagation. The temperature values were given an absolute error of ± 1°C obtained from the product information sheet of the sensors. β was estimated with an absolute error of ± 0.01.

The error of the RH was also taken from the product information sheet of the SHT75 sensor [90]. This error propagation leads to an error in S of ~ 3 % . A detailed list of all instruments in use is given in the Appendix with their corresponding limits and error ranges, see Table 8.6.

4.4 Theoretical Growth Analysis

A comparison between theoretical and experimental growth rates was done for every measurement performed. In Chapter 4.2.2 the procedure on how the deviation is applied was explained. When comparing different activation curves only those measurements with a maximum deviation of $\pm 8\%$ were taken into account. This growth analysis can be seen as a requirement for reliable data.

Figure 4.3 shows a summary of all measurements performed including those that were used by Wlasits et al. (2023) [67]. On the x-axis the RH values inside the humidifier are depicted and on the y-axis the deviation between theoretical and experimental growth. A clear inverse linear trend between RH and deviation is visible. At lower RH the theoretical growth was underestimated so a positive deviation on the supersaturation ratio was applied to approximate the experimental data. With increasing RH the difference between theory and experiment diminishes. The green area presented in Figure 4.3 should denote the error range of the SANC which was calculated to be about 3 %, as shown in Chapter 4.3.

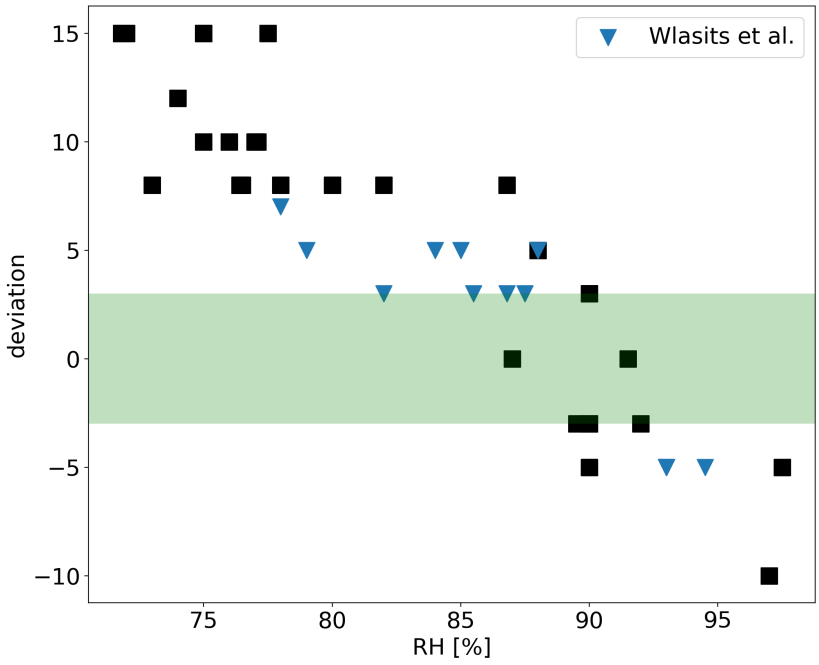

Figure 4.3: Analysis of all performed measurements, comparing RH values inside the humidifier and the deviation between theoretical and experimental growth. Data points marked by the blue triangles are adopted from Wlasits et al. [67]. The green area marks the estimated error of the instrument.

Due to the variable flow rates through the humidifier, an RH sensor was mounted right after the humidifier to monitor the RH. The RH inside the humidifier is dependent on the temperature T_{hum} as well as on the flow rate. The higher the flow rate through the humidifier, the more undersaturated the exiting aerosol was. Additionally, the greater the temperature, the higher the relative humidity. Changes in T_{hum} alters the nucleation temperature, see eq.(3.9) and eq.(3.11). In order to perform measurements at comparable nucleation temperatures the temperature inside the humidifier was altered. The temperature inside the chamber could not be altered as it was already close to room temperature and the expansion valve was limited.

Figure 4.3 shows that measurements were most reliable for an RH value above 85 %. This validates that measurements with SANC should be performed with a (nearly) saturated vapor mixture [46],[80],[81],[91]. The trend to a negative deviation for values above 90 % coincides noticeably with the error on the RH sensor. According to the technical information sheet of the humidity sensor SHT75, the error amounts from ±1.8 % to ±4 % for values above 90% relative humidity [90]. The deviation of -10% for an RH value of 97% is unexpected. Figure 4.3 shows that even-though a desired 100 % RH was not possible, the SANC nonetheless provided reliable data for RH values above 85%. Below 85% a significant difference between

the theoretical growth model and experimental values was observed.

5 | Results and Discussion

The following chapter is divided into two sections. The first section concerns the particle generation and discusses the effect of furnace temperature. Furthermore, the different PNSDs for all the materials used in the study will be shown. The second section contains the results of the measurements performed with the SANC showing and comparing several activation curves.

5.1 Particle Number Size Distributions

In Figure 5.1 the influence of the furnace temperature on the particle generation is depicted. The material under investigation was pPet at 200°C, 220° and 230°C. The distributions were fitted with a lognormal and skewed type-normal function respectively. Details on these fit functions can be found in the previous chapter (Chapter 4). From these functions the maximum value $\bar{x}$, (the mean respectively) as well as the Full Width at Half Maximum (FWHM) were calculated. Table 5.1 shows a summary of the obtained results.

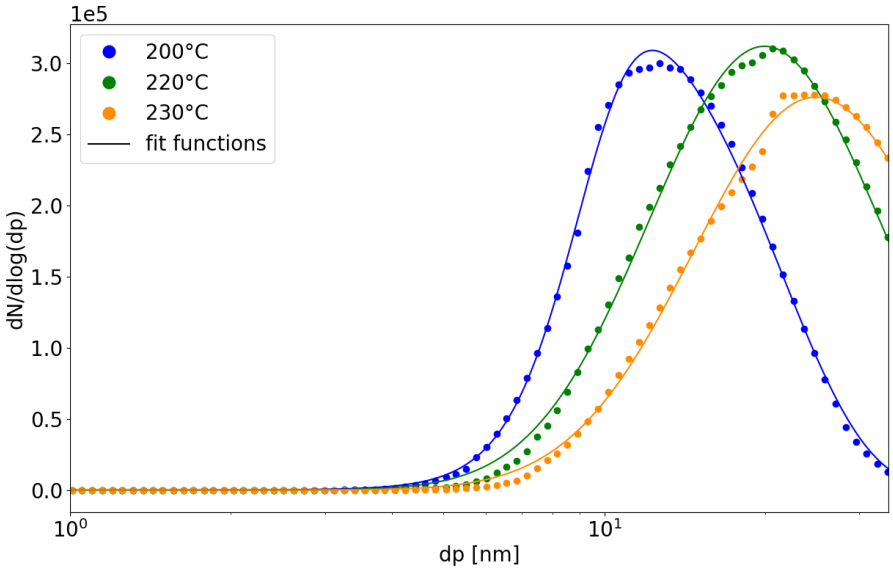

Figure 5.1: Primary PNSDs obtained at three different temperatures. Dots represent the experimental data and the solid lines the fit functions.

It can be seen in Figure 5.1, as well as in Table 5.1, that the generation of nanoplastic particles is temperature dependent. Not only the shape, but also the position of these distributions changes depending on the furnace temperature. Greater temperature leads to a shift of the distribution to larger particle sizes. The absolute shift of the maxima between 200°C and 230°C is about (13 ± 6) nm. The difference in shape is described by the FWHM, which is significantly smaller for the distribution at lower temperature. However, it has to be mentioned that for 220° and for 230°C the right tail of the distribution could not be recorded due to the limitations of the DMA. The maximum applied voltage is 10 000V which considering the geometry of the DMA and the flow rates corresponds to a maxmimum diameter size of about 40nm.

T[°C]	$\bar{x}$ [nm]	FWHM [nm]
200:	12,3 ± 1,7	13,0 ± 1,8
220:	19,9 ± 2,7	24,7 ± 3,3
230:	24,9 ± 3,4	33,0 ± 4,0

Table 5.1: Mean and FWHM of the fitted PNSD for each temperature, corresponding to Figure 5.1.

Overall these observations are in very good agreement with P. Wlasits et al. [31]. Within this paper it was shown that a decreasing temperature led to a shift of the distribution to smaller particle sizes. Furthermore, it was also observed that the shape of the distribution narrows with decreasing temperature. [31]

Figure 5.2 shows the PNSDs of all materials in use. Significant differences can be observed in these distribution. First of all, the range of diameters that is covered differs immensely within the different materials. The material from which the smallest particles are produced are NaCl, then pPet and lastly cPet. Comparing the maximum values and the FWHMs, given in Table 5.2, it is shown that $\bar{x}$ for NaCl and pPet are similar. However, the distribution of NaCl is broader and shifted to smaller sizes.

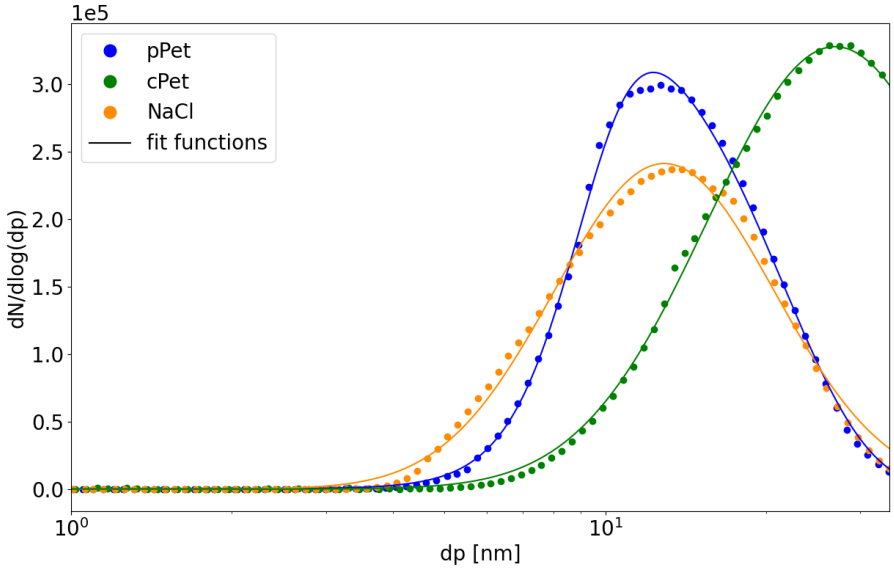

Figure 5.2: Primary PNSDs of the different materials in use. The furnace temperatures are listed together with the maximum value and the width in table 5.2

Compared to pPet and NaCl the distribution of cPet is shifted to larger particle sizes which results in the fact that the whole course of the distribution could not be recorded. Therefore for cPet a large part of the right tail of the distribution is missing. Unfortunately, it was not possible to generate smaller particles, respectively shifting the whole distribution to even smaller sizes.

material	T_f [°C]	$\bar{x}$ [nm]	FWHM [nm]
pPet:	200	12.3 ± 1.7	13.0 ± 1.8
cPet:	200	26.9 ± 2.9	37.0 ± 4.0
NaCl:	667	12.8 ± 1.4	15.2 ± 1.6

Table 5.2: Mean and FWHM of the fitted PNSD for pPet, cPet and NaCl, corresponding to Figure 5.2.

Comparing the distributions of the two thermoplastics, these findings are again in very good agreement with Wlasits et al. (2022) [31]. Herein, it was also shown that the purity version of PET produces smaller particle sizes compared to cPet that is assumed to be chemically enhanced by additives [31].

Discussion

The results of the measurements showed that a significant amount of NPs were generated at moderate temperature (about 200°C). Therefore it can be concluded that any process in which thermoplastics are subject to heat inevitably leads to the formation of NPs (i.e. burning of plastic materials [92] or 3D printing [93]). Stephens et al. (2013) already showed that during the application of commercially available 3D Desktop printers ultra fine particles are produced [93]. Filtering systems within these printers should strongly be considered to prevent potential health risk [93].

One way of tackling the problem of accumulated plastic waste, is the recycling of used plastic products. Two different processes are used to recycle PET: chemical and mechanical recycling [94]. The former relies on the depolymerisation of PET, but has the disadvantage of high costs [94]. The necessary steps for mechanical recycling are: sorting, shredding, washing, drying and melting [95]. Two of these steps are potential sources of microplastics and nanoplastics respectively. First of all, due to mechanical stress micro-sized plastics can occur [23]. But more importantly, melting of the shredded plastic will produce NPs. Therefore a large contribution to the NP and MP concentrations in the atmosphere originating from recycling stations is possible.

5.2 Size Analyzing Nuclei Counter

In the following chapter, several activation curves are compared. Herein, it is important to mention that the activation probability is dependent on several factors, such as particle size, nucleation temperature, charging state and seed particle material [91]. The paper by Wlastis et al. (2023) that was written in course of these measurements focuses on the influence of nucleation temperature on the activation [67]. Therefore this aspect will not be discussed in this thesis.

5.2.1 Calibration

First of all, the integrity of the setup needed to be confirmed. A calibration measurement with sodium chloride, a material that has already been subject to measurements in the past, was performed and compared to established results. The onset saturation ratio S_0 for particles at about 6nm with a nucleation temperature around T_0= 14°C were compared. The activation curve, nucleation probability as a function of saturation ratio, is depicted in Figure 5.3. For the sake of clarity in this and in every following activation curve error bars are excluded.

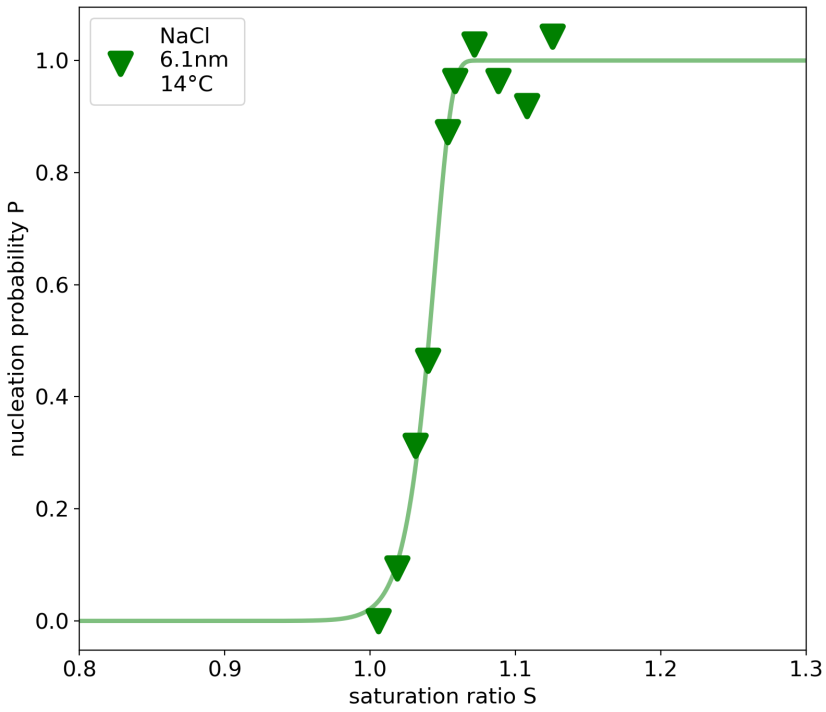

Figure 5.3: Activation curve of NaCl particles at a size of 6.1nm and at a nucleation temperature of around 14°C.

The shown curve exhibits a steep and fast activation. Shortly after the saturation ratio exceeds 1 the activation of the particles already starts. Before S = 1,1 the plateau is already

reached. The obtained S_0 = 1,04 is compared to the results from Kupc et al. (2013) with S_0 = 1,08 [91]. In the table below the exact values of the particle size, nucleation temperature and the onset saturation ratio of the calibration measurement and the measurement of Kupc et al. (2013) are listed. Comparing the onset saturation ratios, the values are within the error range.

	dp [nm]	S0	T0 [°C]
measured:	6,1 ± 0,7	1,04 (+0,08/-0,04)	13,90 ± 0,13
Kupc et al. [91]:	5,7 ± 0,4	1,08 ± 0,01	14,74 ± 0,22

5.2.2 Reproducibility

To check the reproducibility of the measurements, two activation curves at similar experimental conditions were repeated. Figure 5.4 shows two activation curves of pPet with dp = 6,2nm at a nucleation temperature around 7°C.

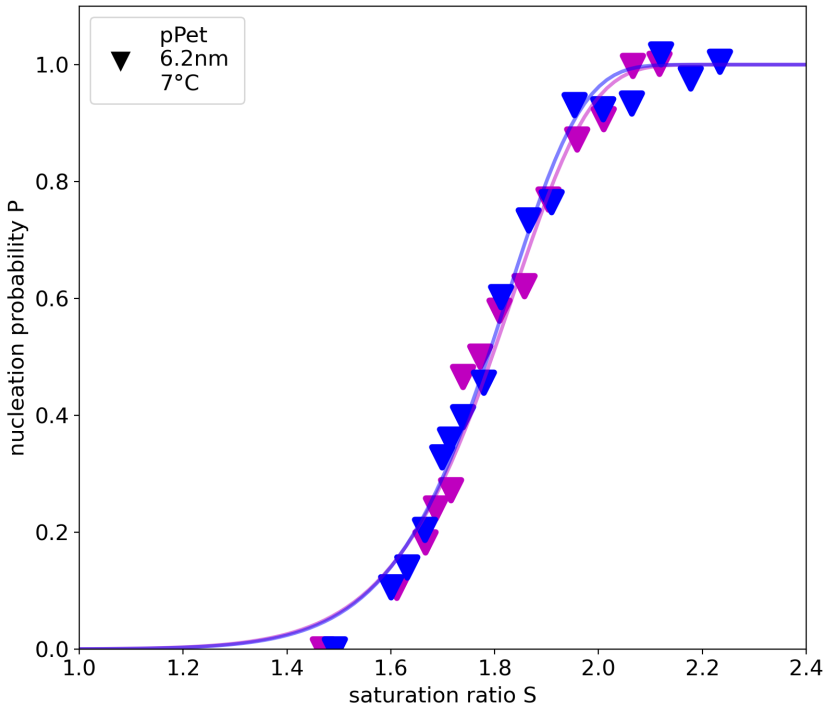

Figure 5.4: Two activation curves at similar experimental conditions confirming the reproducibility of the measurements.

As can be seen in Figure 5.4, the activation curves for both measurements are in very good agreement. In the table below the exact values for the particle size, onset saturation ratio S_0 and nucleation temperature T_0 are listed. When comparing the onset saturation ratio the

values are again well within the error range.

dp [nm]	S0	T0 [°C]
6,2 ± 0,6	1,81 (+0,09/-0,04)	7,52 ± 0,35
6,2 ± 0,6	1,79 (+0,14/-0,04)	7,19 ± 0,30

Compared to the calibration measurement (Figure 5.3), we now have an activation that is less steep. Influences that govern the shape of activation and position on the x-axis will be discussed in the following sections.

5.2.3 Size Effect

After successfully demonstrating the reliability, comparative measurements could be performed. In this next step, the size dependence of the activation was studied. Herein, the activation at three different seed sizes (6nm, 8,5nm and 10nm) at roughly 8°C nucleation temperature was investigated. The results for the activation curves can be seen in Figure 5.5. The activation for particles at dp = 10nm starts earliest and reaches its plateau around S = 1,25. At this saturation ratio no significant activation was observed for 6 nm sized particles. The activation curve of 8,5nm particles is between the curves for nanoplastic particles of 6nm and 10nm size.

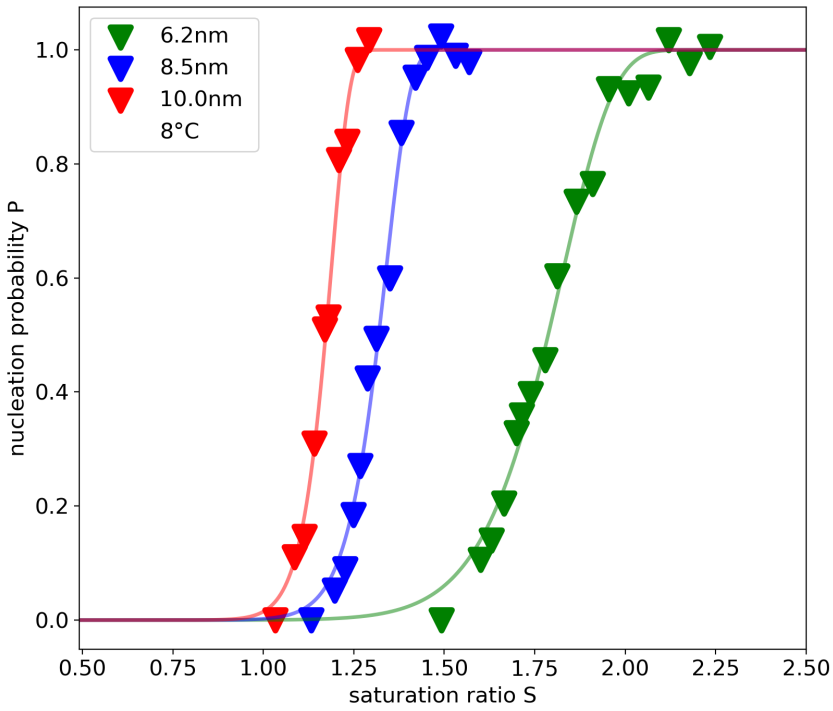

Figure 5.5: Comparison of the activation for different sizes at a nucleation temperature around 8°C.

Summing up, a significant reciprocal dependence of saturation ratio and particle size was observed. This is again in very good agreement with theory (see Fletcher (1958) [96] or as depicted in the Appendix, see Figure 8.1). However, not only a shift to smaller S_0 is visible, but also a change in the slope of the curves can be seen. For particles at 10nm the slope of the activation curve is more pronounced, while the activation curve for particles at 6nm extends over a wider range of saturation ratios. Thus bigger particle sizes lead to a steeper activation curve. In the table below the values for particle size, S_0 and T_0 are listed.

dp [nm]	S0	T0 [°C]
6,2 ± 0,6	1,79 (+0,14/-0,04)	7,19 ± 0,30
8,5 ± 0,8	1,32 (+0,11/-0,04)	7,84± 0,28
10,0 ± 1,4	1,17 (+0,12/-0,03)	8,37 ± 0,26

For these comparisons maintaining a similar nucleation temperature is essential as this also influences the activation behaviour [67]. A limit of T_0 ± 1°C deviation was aimed for when comparing at similar nucleation temperature. The error on the nucleation temperature originates from the fitting procedure.

As introduced in Chapter 4 the Gumbel fit not only provides the onset saturation ratio but also n*, which can be approximated by the number of molecules in the critical cluster [43]. At higher saturation ratio the energy barrier is smaller, which allows the cluster to be smaller in order to reach the size for irreversible growth, see Figure (2.2). This assumption is in line with the retrieved values for n*, which are summarized in the table below. For seed particles with a diameter of 6,2nm the supersaturation need to be higher compared to 8,5nm and 10,0nm. As shown in Figure 2.2 higher supersaturation leads to a smaller critical cluster size. Accordingly, fewer molecules are incorporated into the critical cluster. The retrieved values for n* show an increase with bigger particle sizes.

dp [nm]	n*
6,2 ± 0,6	13 ± 1
8,5 ± 0,8	20 ± 2
10,0 ± 1,4	23 ± 2

Table 5.3: (Approximated) number of molecules inside the critical cluster for different sizes, values were retrieved from the Gumbel fit; given errors followed from the fitting procedure.

For a quantitative determination of n* as number of molecules within the cluster, it is essential to ensure that seed particles are strictly monodisperse [97]. In the performed measurements, however, the resolution of the seed particle size (or rather the mobility equivalent diameter) selection was not precise enough to thoroughly study the critical cluster size. To conduct such measurements it would be advised to employ a high resolution UDMA. Its geometry and its high sheath flow allows to select a narrow range of mobility equivalent diameters [98]. However, the list above should primarily demonstrate the relation that was found between n* and the seed particle size (the onset saturation ratio respectively) and should rather be viewed qualitativey.

5.2.4 Charging Effect

The DMA selects particles according to their electrical mobility resulting in monodispere charged particles [71]. To keep the setup as simple as possible and to avoid unnecessary particle loss no second charger after the mobility selection was mounted. To ensure that the charging state does not affect the extracted parameters, heterogeneous nucleation measurements for particles with and without charge were performed. Two measurements under the same experimental conditions but differentiating in their charging state (negatively charged and neutral) were performed. For this experiment the setup needed to be changed slightly as

explained in Chapter 3.6.

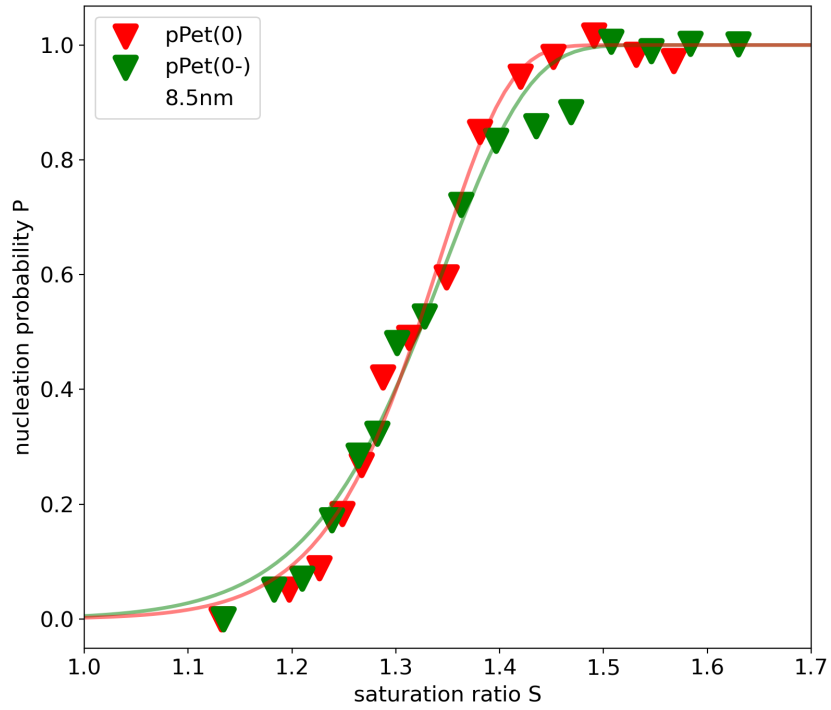

Figure 5.6: Activation curves for neutral seed particles, denoted by (0) and activation curve of charged seed particles (0-). The first measurement was for neutral particles where the neutralizer and the ion trap were turned on. Afterwards both neutralizer and ion trap are turned off and charged particles are measured. Since these measurements were performed consecutively the denotation for the charged particles is given by (0-).

The exact values for the onset saturation ratios and the nucleation temperatures are given in the table below. As seen in Figure 5.6, the activation curves are in very good agreement to each other, indicating that indeed the charging state does not influence the results of the measurements. This is exactly what would be expected from theory. In Chapter 2.3 the effect of the charging states on the saturation ratio was discussed, by introducing the Kelvin-Thomson equation. Comparing with Figure 2.5 at a size of 8.5nm we do not expect any influence of the charging state on the activation behaviour.

8,5 ± 0,7 [nm]	S0	T0 [°C]
neutral:	1,32 (+0,11/-0,04)	7,84 ± 0,28
charged:	1,32 (+0,11/-0,04)	7,81 ± 0,28

In general, measurements were performed for particle sizes between 6nm and 11nm. It is theoretically (Figure 2.5) and experimentally (Figure 5.6) shown that at theses sizes there are

no influences due to the charging state.

5.2.5 Physicochemical Properties

In this section onset saturation ratios for different seed materials are shown. Herein pPet is compared to Ag and NaCl at 4nm at a nucleation temperature around 5°C. The results for Ag and NaCl were adopted from the paper by Kupc et al. (2013) [91]. In Figure 5.7 the left panel shows the activation curve of pPet and S_0 values for Ag and NaCl are added. The right panel compares the onset saturation ratios for different materials in relation to their diameters.

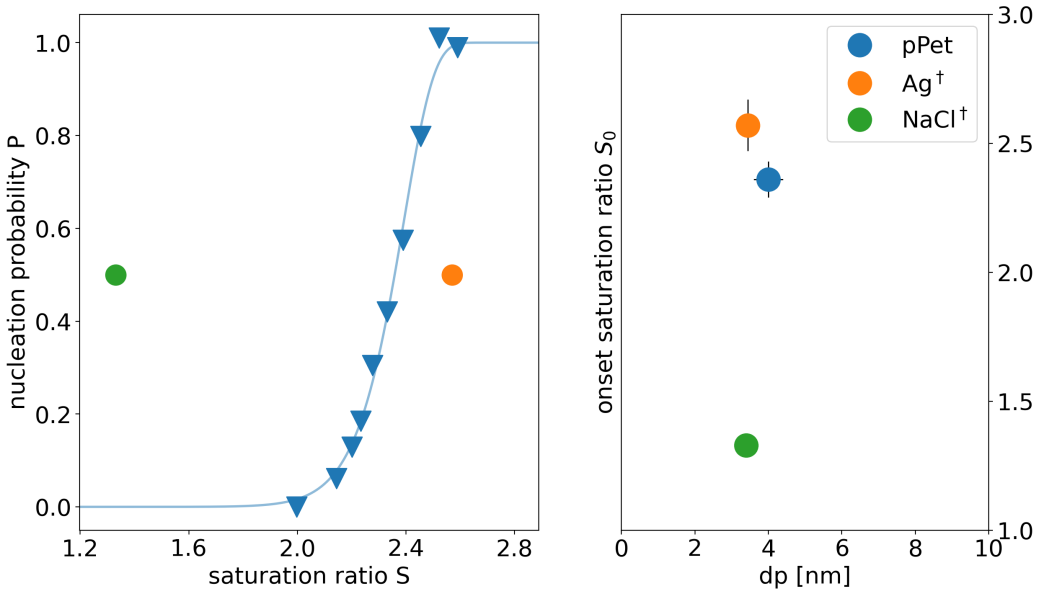

Figure 5.7: Comparison of the onset saturation ratios of NaCl, pPet and Ag at a nucleation temperature around 5°C and at a diameter of about 4nm. In the left panel the activation curve of pPet is presented with inserted S_0 of NaCl and Ag. The right panel shows onset saturation ratios and their diameter. Results that are marked by † correspond to values obtained from Kupc et al. (2013) [91].

The table below shows the exact values for different diameters, nucleation temperatures and the onset saturation ratios for different seed materials.

	dp[nm]	S0	T0 [°C]
pPet(-)	4,1 ± 0,5	2,36 ± 0,11	4,53 ± 0,30
Ag(0)† [91]	3,4 ± 0,3	2,57 ± 0,10	4,85 ± 0,10
NaCl(0)† [91]	3,4 ± 0,3	1,33 ± 0,02	5,09 ± 0,10

As shown NaCl (ionic crystal) has the highest cooperativity, since for this seed material

the lowest saturation ratio are needed for activation. Thus Na^+ seems to favorably react with the partially negatively charged oxygen of the water molecule while hydrogen interacts with Cl^- (charge-dipole interaction).

As shown in Figure 5.7 pPet and Ag need higher onset saturation ratios in order to be activated. Both seed materials have limited solubilities in water [64], [99] (due to unfavorable intermolecular interactions), resulting in poor activation. However a difference in S_0 can still be observed. This can be explained by the polar part of the PET sample, leading to dipole-dipole interactions. As shown in Chapter 3.2.1, PET consists of a highly hydrophobic benzol ring, however, it also has an ester part which is slightly polar. On the other hand, bulk silver is arranged in a face-centered cubic crystal structure and is nonpolar. The difference in activation are in line with the energy (/distance) ranges introduced in Table 2.1. As suggested, the interaction between charge-dipole is stronger than dipole-dipole or induced-dipole interactions which is in line with the finding that the activation occurs earlier (lower saturation ratio) for NaCl than for PET, or Ag respectively. Furthermore, the interaction between two dipoles is stronger compared to induced dipole- dipole interaction. This is also in agreement with the results depicted above that the slightly polar PET has a higher cooperativity compared to the nonpolar silver.

The interaction between vapor and seed material can also be described by the wettability using the contact angle [13]. Hydrophobic materials have larger contact angles and as a result a higher supersaturation is needed for activation [91]. From the experimental data, it can be concluded that salt has the smallest contact angle, followed by pPet and lastly Ag.

In the previous chapter, the influence of charging was discussed. Having a close look at the comparison between Kelvin and Kelvin-Thomson single charge (Chapter 2.3), a significant influence is not expected at 4nm particle size. Also keeping in mind that there is an offset between the geometric diameter and the mobility diameter of about 0.3nm [43]. The mobility diameter is bigger compared to the geometric diameter. Furthermore, Tauber et al. demonstrated no charge influence for NaCl and Ag in n-butanol vapor at particle sizes above 3.5nm [100]. At the presented particle sizes of Ag(0) at 3.44nm and NaCl(0) at 3.4nm compared to pPet(-) a charging effect can not fully be ruled out. However, their relevance can safely be assumed to be negligible. The activation for NaCl in water vapor is at lowest onset saturation ratios. The highest onset saturation ratio is needed for the activation of silver particles. Nanoplastic particles, which are slightly polar but still generally hydrophobic material, is situated between these two and thus promoting further support for the statement of Wlastis et al. that chemically similar aggregates positively influence the activation [76]. The fact, that plastic particles experience lower onset saturation ratios than silver is

confirmed by the additional measurements performed for the paper in course of the thesis [67].

5.2.6 PET Comparison

In a next step, nanoplastic particles originating from two different bulk materials of plastic were investigated: commodity version (cPet) from a plastic bottle and PET of higher purity (pPet). Figure 5.8 shows the activation curve for both plastic types at a size of about 8,5nm and at a nucleation temperature of approximately 8°C.

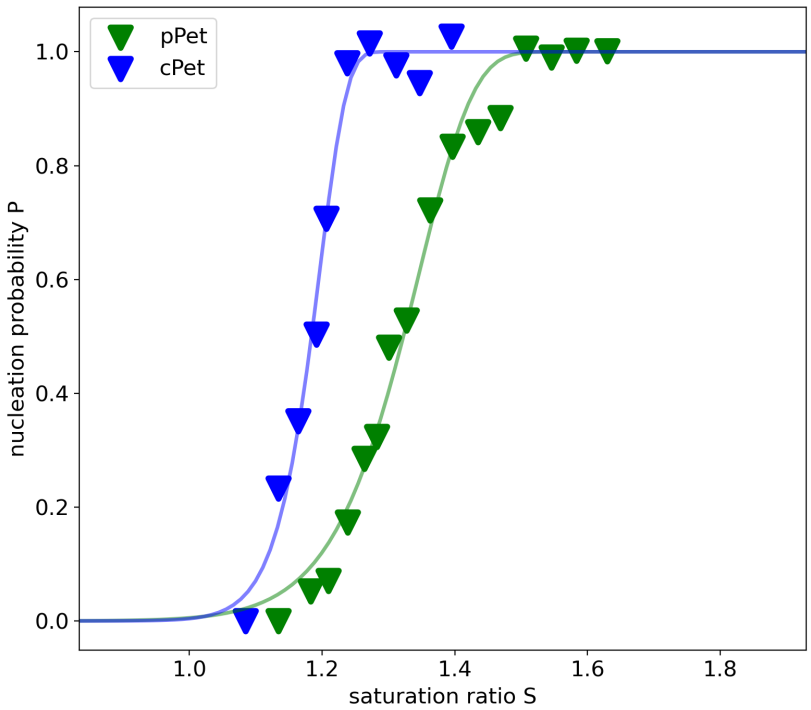

Figure 5.8: Activation for two different plastic types: chemical standard plastic (pPet) compared to commodity plastic (cPet).

Clearly, the activation is different for cPet compared to pPet. Immediately visible is the more cooperative activation of the commodity version. A summary of the exact values can be found in the table below.

	dp [nm]	S0	T0 [°C]
pPet:	8,5 ± 0,7	1,32 (+0,11/-0,04)	7,81 ± 0,28
cPet:	8,6 ± 0,8	1,18 (+0,09/-0,03)	8,12 ± 0,28

Unfortunately, we lack deeper insight into the composition and morphology of both plas-

tic samples. However, there are several possible explanations for the different activation behaviour. Commodity plastics are expected to be altered by additives [23]. The presence of such additives can have multiple possible influences. First of all, chemical entities (molecules/atoms) change the structure of the polymere, which as a result can change the polarity. It can be assumed that commodity plastic has a more heterogeneous surface due to cracks or impurities [101]. These modifications not only increase the polarity of the surface but changes the surface in general, thus suggesting a higher cooperativity. Clearly, more detailed information about surface properties and chemical composition (e.g. stemming from mass spectrometry) is needed to properly interpret the differences in their activation properties.

6 | Conclusion

Within this thesis, the same approach (evaporation of bulk plastics) as employed by Wlasits et al. (2022) was used to generate nanoplastic particles [31]. Two different plastic types were analyzed: commodity Polyethylene terephthalate (cPet) and Polyethylene terephthalate in a purer version (for chemical analysis, pPet). The evaporation of pPet produced smaller nanoparticles compared to cPet.

Heterogeneous nucleation processes were studied by feeding the generated nanoplastic particles into the Size Analyzing Nuclei Counter (SANC). Herein, the activation of seed particles was measured and the onset saturation ratios evaluated. In a first step, the reliability of the setup was verified by performing a calibration measurement and evaluating the reproducibilty of the setup.

It was shown that nano-sized seed particles (made out of bulk plastics by evaporation) were activated and followed the trend predicted by nucleation theory. An expected decrease in onset saturation ratio with increasing seed particles size was successfully demonstrated. Furthermore, it was shown that the charges of seed particles at a size of 8,5nm do not influence the activation behaviour which aligns again with predictions from theory.

The activation properties of different seed particle materials were compared. The materials in question were pPet, sodium chloride (NaCl) and silver (Ag). The activation of nanoplastics was categorized between NaCl and Ag. Seed particles made out of NaCl exhibited activation at lowest S. The different activation behaviour resulted from the chemical compositions and the resulting intermolecular forces between the seed material and water vapor confirming the approach of Wlasits et al. (2020) [76]. However, at the moment this conclusion is still speculative since deeper knowledge of the composition of the plastic material in use is missing.

A significant difference in onset saturation ratio for cPet and pPet was found. Seed particles made out of commodity plastic experienced an activation at lower saturation ratios. The origin of this difference is manifold. Chemical compositions are assumed to vary due to the addition of additives. This incorporation of atoms/molecules has an influence on the

chemical composition. Furthermore, surface details of both materials are unknown. However, it is assumed that commodity Pet is more surface sensitive and impurities led to an increased surface available for water vapor molecules to nucleate on.

In conclusion, this thesis provided a valuable database for further research in the future.

7 | Future Research

The performed measurements showed that nanoplastic particles (that were generated using a tube furnace) acted as seed particles for heterogeneous nucleation of water vapor. Possible future research ideas and questions that need to be answered are as follows:

1. **Properties of nanoplastic particles:** knowledge about particle surface structure, shape, composition etc.
2. **Concentration measurement:** knowledge about particle number size distribution of plastic particles in the atmosphere
3. **Measurements at lower temperatures:** simulating atmospheric conditions, SANC measurements at lower conditions

Properties of nanoplastic particles

In general, we lack information about the chemical composition of the particle surface, its structure and the general shape of the particles that were generated by evaporation using the tube furnace. As mentioned, the commodity PET version was retrieved from a plastic bottle. However, no information on the composition is available. To better understand the potential relevance more detailed physico-chemical analysis would be required (i.e. mass spectrometry). Furthermore, experiments involving different plastic materials, such as PP or PE could be envisaged to access the relevance of chemical composition on activation properties, as evidenced by the difference in activation behaviour between the purity and the commodity version.

Another source of uncertainty is the lack in information how different methods employed to convert bulk plastic material to nanosize range nucleation particles affect the surface structure and subsequently the activation behavior. Different sources (heat or mechanical stress e.g.) are very likely to have an influence on the general shape as well as on the surface properties [102]. NPs and MPs stay in the atmosphere over a large time span. They are continuously exposed to external influences, such as solar radiation, mechanical stress (further fragmentation) and/or chemical stress (interaction with e.g. acids) [101]. These influences considerably affect the seeding properties (efficiencies) of the particles. For instance, aging

leads to roughness in the surface structure which might lead to an enhanced activation due to an improved number of active sites [101]. To investigate the question how aging affects the activation behaviour similar SANC experiments could be performed with test particles that were intentionally altered e.g. by UV radiation.

Concentration measurements

The existence of plastic particles within the atmosphere is evident. However, their exact concentration remains unknown. Common instruments that are used for concentration measurements of plastic rely on visual examination or spectroscopic analysis methodologies (e.g. FTIR, Raman) [103]. The main limitation of the instruments used for the determination of the concentration of plastic particles in the atmosphere is the lower detection limit [104] ($\sim$ 20 μm for μFTIR [103]). The results obtained in the thesis convincingly showed that at moderate furnace temperatures significant amounts of nanoplastic particles are generated. This is particularly relevant as melting and reshaping of thermoplastic is a widely used method in the recycling industrie as well as in 3D printers. This is not only hazardous to human health and calls for adequate filtering systems to avoid potential inhalation of NPs or MPs but also suggests that the concentration of NPs and MPs in the atmosphere is largely underestimated.

Measurements at lower temperatures

Experiments in this thesis and in the study by Wlasits et al. (2023) discussing the influence of the nucleation temperature on the activation were performed in a range of about 6 to 16°C [67]. Clouds are formed at high altitudes where temperatures are much lower. Therefore experiments at similar conditions should be performed in order to properly estimate the putative atmospheric influence of plastic particles. Furthermore, the influence of nanoplastics acting as ice nucleation particles should be investigated. As stated by Aeschlimann et al. (2022), hydrophobicity of seed particles minimizes the probability of NPs to act as CCN [101]. However, this property becomes less influential for seed particles promoting ice nucleation [101]. Therefore as suggested by Aeschlimann et al. (2022) NPs might have more potential to act as INPs .

Bibliography

[1] "History of the ipcc." `https://www.ipcc.ch/about/history/`. Accessed: 2023-05-09.

[2] T. Stocker, D. Qin, G.-K. Plattner, L. Alexander, S. Allen, N. Bindoff, F.-M. Bréon, J. Church, U. Cubasch, S. Emori, P. Forster, P. Friedlingstein, J. G. N. Gillett, D. Hartmann, E. Jansen, B. Kirtman, R. Knutti, K. K. Kumar, P. Lemke, J. Marotzke, V. Masson-Delmotte, G. Meehl, I. Mokhov, S. Piao, V. Ramaswamy, D. Randall, M. Rhein, M. Rojas, C. Sabine, D. Shindell, L. Talley, D. Vaughan, and S.-P. Xie, "Technical Summary," in *Climate Change 2013: The Physical Science Basis. Contribution of Working Group I to the Fifth Assessment Report of the Intergovernmental Panel on Climate Change [Stocker, T.F., D. Qin, G.-K. Plattner, M. Tignor, S.K. Allen, J. Boschung, A. Nauels, Y. Xia, V. Bex and P.M. Midgley (eds.)]*, p. 33–115, United Kingdom and New York, NY, USA: Cambridge University Press, Cambridge, 2013.

[3] N. Bellouin, "Aerosols | role in climate change," in *Encyclopedia of Atmospheric Sciences (Second Edition)* (G. R. North, J. Pyle, and F. Zhang, eds.), pp. 76–85, Oxford: Academic Press, second edition ed., 2015.

[4] P. Forster, V. Ramaswamy, P. Artaxo, T. Berntsen, R. Betts, D. Fahey, J. Haywood, J. Lean, D. Lowe, G. Myhre, J. Nganga, R. Prinn, G. Raga, M. Schulz, and R. V. Dorland, "Changes in Atmospheric Constituents and in Radiative Forcing," in *Climate Change 2007: The Physical Science Basis. Contribution of Working Group I to the Fourth Assessment Report of the Intergovernmental Panel on Climate Change [Solomon, S., D. Qin, M. Manning, Z. Chen, M. Marquis, K.B. Averyt, M.Tignor and H.L. Miller (eds.)]*, pp. 131–234, United Kingdom and New York, NY, USA: Cambridge University Press, Cambridge, 2007.

[5] O. Boucher, D. Randall, P. Artaxo, C. Bretherton, G. Feingold, P. Forster, V.-M. Kerminen, Y. Kondo, H. Liao, U. Lohmann, P. Rasch, S. Satheesh, S. Sherwood, B. Stevens, and X. Zhang, "Clouds and Aerosols," in *Climate Change 2013: The Physical Science Basis. Contribution of Working Group I to the Fifth Assessment Report of the Intergovernmental Panel on Climate Change [Stocker, T.F., D. Qin, G.-K. Plattner, M. Tignor,*

S.K. Allen, J. Boschung, A. Nauels, Y. Xia, V. Bex and P.M. Midgley (eds.)], United Kingdom and New York, NY, USA: Cambridge University Press, (2013).

[6] P. Forster, T. Storelvmo, K. Armour, W. Collins, J.-L. Dufresne, D. Frame, D. Lunt, T. Mauritsen, M. Palmer, M. Watanabe, M. Wild, and H. Zhang, "The Earth's Energy Budget, Climate Feedbacks, and Climate Sensitivity," in *Climate Change 2021: The Physical Science Basis. Contribution of Working Group I to the Sixth Assessment Report of the Intergovernmental Panel on Climate Change* (V. Masson-Delmotte, P. Zhai, A. Pirani, S. Connors, C. Péan, S. Berger, N. Caud, Y. Chen, L. Goldfarb, M. Gomis, M. Huang, K. Leitzell, E. Lonnoy, J. Matthews, T. Maycock, T. Waterfield, O. Yelekçi, R. Yu, and B. Zhou, eds.), p. 923–1054, Cambridge, United Kingdom and New York, NY, USA: Cambridge University Press, 2021.

[7] W. C. Hinds, "Atmospheric Aerosols," in *Aerosol technology : properties, behavior, and measurement of airborne particles*, ch. 14, pp. 304–315, New York: John Wiley Sons, Ins., second edition. ed., 1999.

[8] H. Vehkamäki, *Classical Nucleation Theory in Multicomponent Systems*. Springer, 2006.

[9] J. H. Seinfeld and S. N. Pandis, "Nucleation," in *Atmospheric chemistry and physics : from air pollution to climate change* (Wiley, ed.), ch. 11, pp. 448–492, Hoboken, New Jersey: Wiley, 2016.

[10] W. C. Hinds, "Condensation and Evaporation," in *Aerosol technology : properties, behavior, and measurement of airborne particles*, ch. 13, pp. 278–303, New York: John Wiley Sons, Ins., second edition. ed., 1999.

[11] BiologyReader, "Cloud formation." `https://biologyreader.com/cloud-formation.html`, 2022. [Online; accessed June-2022].

[12] U. Lohmann, F. Lüönd, and F. Mahrt, "Clouds," in *An Introduction to Clouds: From the Microscale to Climate*, p. 1–25, Cambridge University Press, 2016.

[13] U. Lohmann, F. Lüönd, and F. Mahrt, "Microphysical processes in cold clouds," in *An Introduction to Clouds: From the Microscale to Climate*, p. 218–250, Cambridge University Press, 2016.

[14] J. H. Seinfeld and S. N. Pandis, "Global Climate," in *Atmospheric chemistry and physics : from air pollution to climate change* (Wiley, ed.), ch. 23, pp. 931–969, Hoboken, New Jersey: Wiley, 2016.

[15] U. Lohmann, F. Lüönd, and F. Mahrt, "Atmospheric aerosol particles," in *An Introduction to Clouds: From the Microscale to Climate*, p. 115–154, Cambridge University Press, 2016.

[16] U. Lohmann, F. Lüönd, and F. Mahrt, "Impact of aerosol particles and clouds on climate," in *An Introduction to Clouds: From the Microscale to Climate*, p. 335–367, Cambridge University Press, 2016.

[17] D. W. Fahey, S. Doherty, K. A. Hibbard, A. Romanou, and P. C. Taylor, "Physical drivers of climate change," Climate Science Special Report: Fourth National Climate Assessment, Volume I, pp. 73–113, Washington, DC, USA: U.S. Global Change Research Program, 2017. 0615b4ff-d185-4e14-9d4d-5bea1ce6ca51.

[18] M. Vert, Y. Doi, K.-H. Hellwich, M. Hess, P. Hodge, P. Kubisa, M. Rinaudo, and F. Schué, "Terminology for biorelated polymers and applications (iupac recommendations 2012)," *Pure and Applied Chemistry*, vol. 84, no. 2, pp. 377–410, 2012.

[19] J. Frias and R. Nash, "Microplastics: Finding a consensus on the definition," *Marine Pollution Bulletin*, vol. 138, pp. 145–147, 2019.

[20] J. P. da Costa, P. S. Santos, A. C. Duarte, and T. Rocha-Santos, "(nano)plastics in the environment – sources, fates and effects," *Science of The Total Environment*, vol. 566-567, pp. 15–26, 2016.

[21] R. Geyer, J. R. Jambeck, and K. L. Law, "Production, use, and fate of all plastics ever made," *Science Advances*, vol. 3, no. 7, p. e1700782, 2017.

[22] A. Chamas, H. Moon, J. Zheng, Y. Qiu, T. Tabassum, J. H. Jang, M. Abu-Omar, S. L. Scott, and S. Suh, "Degradation Rates of Plastics in the Environment," *ACS Sustainable Chemistry & Engineering*, vol. 8, pp. 3494–3511, Mar 2020.

[23] M. Cole, P. Lindeque, C. Halsband, and T. S. Galloway, "Microplastics as contaminants in the marine environment: A review," *Marine Pollution Bulletin*, vol. 62, no. 12, pp. 2588–2597, 2011.

[24] C. M. Rochman, "Microplastics research-from sink to source," *Science*, vol. 360, no. 6384, pp. 28–29, 2018.

[25] R. Dris, J. Gasperi, M. Saad, C. Mirande, and B. Tassin, "Synthetic fibers in atmospheric fallout: A source of microplastics in the environment?," *Marine Pollution Bulletin*, vol. 104, no. 1, pp. 290–293, 2016.

[26] A. R. Aves, L. E. Revell, S. Gaw, H. Ruffell, A. Schuddeboom, N. E. Wotherspoon, M. LaRue, and A. J. McDonald, "First evidence of microplastics in Antarctic snow," *The Cryosphere*, vol. 16, no. 6, pp. 2127–2145, 2022.

[27] O. Alabi, K. Ologbonjaye, O. Awosolu, and O. Alalade, "Public and Environmental Health Effects of Plastic Wastes Disposal: A Review," *Journal of Toxicology and Risk Assessment*, vol. 5, 04 2019.

[28] M. Kazemi, S. Faisal Kabir, and E. H. Fini, "State of the art in recycling waste thermoplastics and thermosets and their applications in construction," *Resources, Conservation and Recycling*, vol. 174, p. 105776, 2021.

[29] S. Kazemi Najafi, "Use of recycled plastics in wood plastic composites – a review," *Waste Management*, vol. 33, no. 9, pp. 1898–1905, 2013.

[30] S. Chowdhury, A. T. Maniar, and O. Suganya, "Polyethylene terephthalate (pet) waste as building solution," 2013.

[31] P. J. Wlasits, A. Stoellner, G. Lattner, K. Maggauer, and P. M. Winkler, "Size characterization and detection of aerosolized nanoplastics originating from evaporated thermoplastics," *Aerosol Science and Technology*, vol. 56, no. 2, pp. 176–185, 2022.

[32] J. Bourgalais, V. Roussel, M. Capron, A. Benidar, A. Jasper, S. Klippenstein, L. Biennier, and S. Picard, "Low Temperature Kinetics of the First Steps of Water Cluster Formation," *Physical Review Letters*, vol. 116, 03 2016.

[33] U. Lohmann, F. Lüönd, and F. Mahrt, "Cloud droplet formation and Köhler theory," in *An Introduction to Clouds: From the Microscale to Climate*, p. 155–185, Cambridge University Press, 2016.

[34] H. Vehkamäki and I. Riipinen, "Thermodynamics and kinetics of atmospheric aerosol particle formation and growth," *Chem. Soc. Rev.*, vol. 41, pp. 5160–5173, 2012.

[35] U. Lohmann, F. Lüönd, and F. Mahrt, "Thermodynamics," in *An Introduction to Clouds: From the Microscale to Climate*, p. 26–67, Cambridge University Press, 2016.

[36] P. M. Winkler, *Experimental study of condensation processes in systems of water and organic vapors employing an expansion chamber.* PhD thesis, University of Vienna, 2004.

[37] J. H. Seinfeld and S. N. Pandis, "Thermodynamics of Aerosols," in *Atmospheric chemistry and physics : from air pollution to climate change* (Wiley, ed.), ch. 10, pp. 396–447, Hoboken, New Jersey: Wiley, 2016.

[38] N. H. Fletcher and P. Squires, *The physics of rainclouds / N.H. Fletcher ; with an introductory chapter by P. Squires and a foreword by E.G. Bowen.* Cambridge University Press London, 1962.

[39] T. Pinterich, *Developement of a versatile size analyzing nuclei counter (vSANC) and application to ambient aerosol studies.* PhD thesis, University of Vienna, 2015.

[40] H. Vehkamäki, A. Määttänen, A. Lauri, M. Kulmala, P. Winkler, A. Vrtala, and P. E. Wagner, "Heterogeneous multicomponent nucleation theorems for the analysis of nanoclusters," *J Chem Phys*, vol. 126, p. 174707, May 2007.

[41] L. Makkonen, "Young's equation revisited," *Journal of physics. Condensed matter : an Institute of Physics journal*, vol. 28, p. 135001, 03 2016.

[42] A. Määttänen, H. Vehkamäki, A. Lauri, S. Merikallio, J. Kauhanen, H. Savijärvi, and M. Kulmala, "Nucleation studies in the Martian atmosphere," *Journal of Geophysical Research: Planets*, vol. 110, no. E2, 2005.

[43] P. M. Winkler and P. E. Wagner, "Characterization techniques for heterogeneous nucleation from the gas phase," *Journal of Aerosol Science*, vol. 159, p. 105875, 2022.

[44] D. Kashchiev, "Forms and applications of the nucleation theorem," *The Journal of Chemical Physics*, vol. 125, 07 2006. 014502.

[45] D. Kashchiev, "On the relation between nucleation work, nucleus size, and nucleation rate," *The Journal of Chemical Physics*, vol. 76, pp. 5098–5102, 05 1982.

[46] C. Tauber, X. Chen, P. Wagner, P. Winkler, C. Hogan, and A. Maisser, "Heterogeneous Nucleation onto Monoatomic Ions: Support for the Kelvin-Thomson Theory," *ChemPhysChem*, vol. 19, 09 2018.

[47] T. Kihara, *Intermolecular Forces*. Wiley, 1976.

[48] P. W. Atkins, *Physikalische Chemie*. Weinheim: VCH, 1996.

[49] J. N. Israelachvili, "4 - Interactions Involving Polar Molecules," in *Intermolecular and Surface Forces (Third Edition)*, pp. 71–90, San Diego: Academic Press, third ed., 2011.

[50] R. J. Ouellette and J. D. Rawn, "1 - Structure of Organic Compounds," in *Principles of Organic Chemistry* (R. J. Ouellette and J. D. Rawn, eds.), pp. 1–32, Boston: Elsevier, 2015.

[51] E. M. Aldred, C. Buck, and K. Vall, "Chapter 3 - Bonds found in biological chemistry," in *Pharmacology* (E. M. Aldred, C. Buck, and K. Vall, eds.), pp. 11–19, Edinburgh: Churchill Livingstone, 2009.

[52] Jmol development team, "Jmol."

[53] J. N. Israelachvili, "5 - Interactions Involving the Polarization of Molecules," in *Intermolecular and Surface Forces (Third Edition)*, pp. 91–106, San Diego: Academic Press, third ed., 2011.

[54] J. N. Israelachvili, "2 - Thermodynamic and Statistical Aspects of Intermolecular Forces," in *Intermolecular and Surface Forces (Third Edition)*, pp. 23–51, San Diego: Academic Press, third ed., 2011.

[55] E. Stauffer, J. A. Dolan, and R. Newman, "Chapter 3 - Review of Basic Organic Chemistry," in *Fire Debris Analysis* (E. Stauffer, J. A. Dolan, and R. Newman, eds.), pp. 49–83, Burlington: Academic Press, 2008.

[56] P. Atkins and J. de Paula, "Molecular structure," in *Physical Chemistry*, ch. 11, pp. 362–403, New York: W.H. Freeman and Company, 8th edition. ed., 2006.

[57] R. Gillespie, "Fifty years of the vsepr model," *Coordination Chemistry Reviews*, vol. 252, no. 12, pp. 1315–1327, 2008.

[58] "Introduction," Non-Covalent Interactions in Proteins, pp. 1–26, WORLD SCIENTIFIC, Sep 2020.

[59] J. N. Israelachvili, "3 - Strong Intermolecular Forces: Covalent and Coulomb Interactions," in *Intermolecular and Surface Forces (Third Edition)*, pp. 53–70, San Diego: Academic Press, third ed., 2011.

[60] L. Schaeffer, "Chapter 14 - The Role of Functional Groups in Drug–Receptor Interactions," in *The Practice of Medicinal Chemistry (Fourth Edition)* (C. G. Wermuth, D. Aldous, P. Raboisson, and D. Rognan, eds.), pp. 359–378, San Diego: Academic Press, fourth edition ed., 2008.

[61] R. B. Silverman and M. W. Holladay, "Chapter 3 - receptors," in *The Organic Chemistry of Drug Design and Drug Action (Third Edition)* (R. B. Silverman and M. W. Holladay, eds.), pp. 123–163, Boston: Academic Press, third edition ed., 2014.

[62] J. N. Israelachvili, "6 - Van der Waals Forces," in *Intermolecular and Surface Forces (Third Edition)*, pp. 107–132, San Diego: Academic Press, third ed., 2011.

[63] J. Speight, "Monomers, Polymers, and Plastics," ch. 11, pp. 499–537, 12 2011.

[64] Sigma-Aldrich, *SAFETY DATA SHEET*, 4 2022. Version 6.3.

[65] R. Smith, H. Inomata, and C. Peters, "Chapter 4 - historical background and applications," in *Introduction to Supercritical Fluids* (R. Smith, H. Inomata, and C. Peters, eds.), vol. 4 of *Supercritical Fluid Science and Technology*, pp. 175–273, Elsevier, 2013.

[66] P. Gonugunta, S. Vivekanandhan, A. Mohanty, and M. Misra, "A Study on Synthesis and Characterization of Biobased Carbon Nanoparticles from Lignin," *World Journal of Nano Science and Engineering*, vol. 2, pp. 148–153, 01 2012.

[67] P. J. Wlasits, R. Konrat, and P. M. Winkler, "Heterogeneous Nucleation of Supersaturated Water Vapor onto Sub-10 nm Nanoplastic Particles," *Environmental Science & Technology*, vol. 57, pp. 1584–1591, Jan 2023.

[68] W. C. Hinds, "Electrical Properties," in *Aerosol technology : properties, behavior, and measurement of airborne particles*, ch. 15, pp. 316–348, New York: John Wiley Sons, Ins., second edition. ed., 1999.

[69] N. A. Fuchs, "On the stationary charge distribution on aerosol particles in a bipolar ionic atmosphere," *Geofisica pura e applicata*, vol. 56, pp. 185–193, Sep 1963.

[70] A. Wiedensohler, "An approximation of the bipolar charge distribution for particles in the submicron size range," *Journal of Aerosol Science*, vol. 19, no. 3, pp. 387–389, 1988.

[71] R. C. Flagan, "Electrical Mobility Methods for Submicrometer Particle Characterization," in *Aerosol measurement : principles, techniques, and applications*, ch. 15, pp. 339–364, John Wiley Sons, Ltd, 2011.

[72] G. Steiner, *High Resolution Mobility Spectrometry Of Molecular Ions And Their Effect On The Charging Probabilities Of Airborne Particles Under Bipolar Diffusion Charging Conditions*. PhD thesis, University of Vienna, 2011.

[73] R. C. Flagan, "On differential mobility analyzer resolution," *Aerosol Science and Technology*, vol. 30, no. 6, pp. 556–570, 1999.

[74] Y.-S. Cheng, "Condensation Particle Counters," in *Aerosol measurement : principles, techniques, and applications*, ch. 17, pp. 381–392, John Wiley Sons, Ltd, 2011.

[75] TSI, *Model 3776 Ultrafine Condensation Particle Counter - Operation and Service Manual*. TSI Incorporated.

[76] P. J. Wlasits, D. Stolzenburg, C. Tauber, S. Brilke, S. H. Schmitt, P. M. Winkler, and D. Wimmer, "Counting on chemistry: laboratory evaluation of seed-material-dependent detection efficiencies of ultrafine condensation particle counters," *Atmospheric Measurement Techniques*, vol. 13, no. 7, pp. 3787–3798, 2020.

[77] S. Dhaniyala, M. Fierz, J. Keskinen, and M. Marjamäki, *Instruments Based on Electrical Detection of Aerosols*, ch. 18, pp. 393–416. John Wiley Sons, Ltd, 2011.

[78] TSI, *Aerosol Electrometer - Model 3068B*. TSI Incorporated.

[79] J. Porstendörfer, H. G. Scheibel, F. G. Pohl, O. Preining, G. Reischl, and P. E. Wagner, "Heterogeneous Nucleation of Water Vapor on Monodispersed Ag and NaCl Particles with Diameters Between 6 and 18 nm," *Aerosol Science and Technology*, vol. 4, no. 1, pp. 65–79, 1985.

[80] P. Winkler, A. Vrtala, R. Rudolf, P. Wagner, I. Riipinen, T. Vesala, K. Lehtinen, Y. Viisanen, and M. Kulmala, "Condensation of water vapor: Experimental determination of mass and thermal accommodation coefficients," *Journal of Geophysical Research*, vol. 111, 10 2006.

[81] P. E. Wagner, "A constant-angle mie scattering method (cams) for investigation of particle formation processes," *Journal of Colloid and Interface Science*, vol. 105, no. 2, pp. 456–467, 1985.

[82] O. Preining, P. Wagner, F. Pohl, and W. Szymanski, "Heterogeneous nucleation and droplet growth," in *Aerosol Research at the institute for experimental physics of the university of vienna*, 1981.

[83] Lauda, "Operating instructions - compact low temperature thermostats." `https://www.manualslib.com/manual/1000038/Lauda-Rm-6-T.html#manual`, 1996. [Online; accessed May-2023].

[84] Lauda, "Betriebsanleitung - lauda-compact-kaltethermostate." `https://manualzz.com/doc/4443917/betriebsanleitung`, 2002. [Online; accessed May-2023].

[85] Lauda, "Lauda™ Variocool VC 1200 Process Thermostat with CEE7/7 Plug." `https://www.fishersci.de/shop/products/variocool-vc-1200-process-thermostat-cee7-7-plug-6/16883600`. [Online; accessed May-2023].

[86] W. C. Hinds, "Particle Size Statistics," in *Aerosol technology : properties, behavior, and measurement of airborne particles*, ch. 4, pp. 75–110, New York: John Wiley Sons, Ins., second edition. ed., 1999.

[87] E. Knutson and K. Whitby, "Aerosol classification by electric mobility: apparatus, theory, and applications," *Journal of Aerosol Science*, vol. 6, no. 6, pp. 443–451, 1975.

[88] M. Stolzenburg and P. McMurry, "Equations Governing Single and Tandem DMA Configurations and a New Lognormal Approximation to the Transfer Function," *Aerosol Science and Technology - AEROSOL SCI TECH*, vol. 42, pp. 421–432, 04 2008.

[89] P. M. Winkler, R. L. McGraw, P. S. Bauer, C. Rentenberger, and P. E. Wagner, "Direct determination of three-phase contact line properties on nearly molecular scale," *Sci Rep*, vol. 6, p. 26111, May 2016.

[90] Sensirion, "Datasheet SHT7x." `https://www.sensirion.com/media/documents/9A2ADC83/61642805/Sensirion_Humidity_Sensors_SHT7x_Datasheet.pdf`, 2011. [Online; accessed April-2023].

[91] A. Kupc, P. M. Winkler, A. Vrtala, and P. E. Wagner, "Unusual Temperature Dependence of Heterogeneous Nucleation of Water Vapor on Ag Particles," *Aerosol Science and Technology*, vol. 47, no. 9, pp. i–iv, 2013.

[92] Y. Luo, C. T. Gibson, C. Chuah, Y. Tang, Y. Ruan, R. Naidu, and C. Fang, "Fire releases micro- and nanoplastics: Raman imaging on burned disposable gloves," *Environmental Pollution*, vol. 312, p. 120073, 2022.

[93] B. Stephens, P. Azimi, Z. El Orch, and T. Ramos, "Ultrafine particle emissions from desktop 3d printers," *Atmospheric Environment*, vol. 79, pp. 334–339, 2013.

[94] F. Awaja and D. Pavel, "Recycling of PET," *European Polymer Journal*, vol. 41, no. 7, pp. 1453–1477, 2005.

[95] F. Welle, "Twenty years of PET bottle to bottle recycling—an overview," *Resources, Conservation and Recycling*, vol. 55, no. 11, pp. 865–875, 2011.

[96] N. H. Fletcher, "Size Effect in Heterogeneous Nucleation," *The Journal of Chemical Physics*, vol. 29, no. 3, pp. 572–576, 1958.

[97] P. M. Winkler, A. Vrtala, G. Steiner, D. Wimmer, H. Vehkamäki, K. E. J. Lehtinen, G. P. Reischl, M. Kulmala, and P. E. Wagner, "Quantitative Characterization of Critical Nanoclusters Nucleated on Large Single Molecules," *Phys. Rev. Lett.*, vol. 108, p. 085701, Feb 2012.

[98] G. Steiner, M. Attoui, D. Wimmer, and G. P. Reischl, "A Medium Flow, High-Resolution Vienna DMA Running in Recirculating Mode," *Aerosol Science and Technology*, vol. 44, no. 4, pp. 308–315, 2010.

[99] Sigma-Aldrich, *SAFETY DATA SHEET*, 4 2023. Version 6.6.

[100] C. Tauber, S. Brilke, P. J. Wlasits, P. S. Bauer, G. Köberl, G. Steiner, and P. M. Winkler, "Humidity effects on the detection of soluble and insoluble nanoparticles in butanol operated condensation particle counters," *Atmospheric Measurement Techniques*, vol. 12, no. 7, pp. 3659–3671, 2019.

[101] M. Aeschlimann, G. Li, Z. A. Kanji, and D. M. Mitrano, "Potential impacts of atmospheric microplastics and nanoplastics on cloud formation processes," *Nature Geoscience*, vol. 15, pp. 967–975, Dec 2022.

[102] J. Gigault, A. ter Halle, M. Baudrimont, P.-Y. Pascal, F. Gauffre, T.-L. Phi, H. El Hadri, B. Grassl, and S. Reynaud, "Current opinion: What is a nanoplastic?," *Environmental Pollution*, vol. 235, pp. 1030–1034, 2018.

[103] Y. Zhang, S. Kang, S. Allen, D. Allen, T. Gao, and M. Sillanpää, "Atmospheric microplastics: A review on current status and perspectives," *Earth-Science Reviews*, vol. 203, p. 103118, 2020.

[104] A. Bianco and M. Passananti, "Atmospheric Micro and Nanoplastics: An Enormous Microscopic Problem," *Sustainability*, vol. 12, no. 18, 2020.

[105] Sigma-Aldrich, *SAFETY DATA SHEET*, 2 2021. Version 6.4.

[106] Sigma-Aldrich, *Specification*, 7 2023.

[107] Nabertherm, "Laboratory Furnaces." `https://nabertherm.com/sites/default/files/2022-04/laboratory_english_3.pdf`, 2022. [Online; accessed May-2023].

[108] TSI, *Advanced Aerosol Neutralizer Model 3088*, 4 2020.

[109] M. Qian and J. Ma, "Heterogeneous nucleation on convex spherical substrate surfaces: A rigorous thermodynamic formulation of Fletcher's classical model and the new perspectives derived," *The Journal of Chemical Physics*, vol. 130, 06 2009. 214709.

8 | Appendix

material	CAS-Nr.	melting point
pPet	25038-59-9	250°C-255°C [64]
cPet	no information available	
NaCl	7647-14-5	801°C [105]
Silver	7440-22-4	960°C [99]
water (HPLC Plus)	7732-18-5 [106]	x

Table 8.1: Technical information of the materials used in the measurements.

	R_1 [mm]	R_2 [mm]	L [mm]
alu	18	25	15
st.st.	17.15	24.1	15

Table 8.2: Specifications for die aluminium Vienna type DMA and the stainless steel Vienna type DMA.

A_1	A_2	A_3	A_4	A_5
77.34491296	7235.424651	0	8.2	0.0057113

Table 8.3: Coefficients to calculate the saturation equilibrium vapor pressure for water using eq.(4.5) [36].

t_{flush}	15 s
t_{delay}	10 s
t_{exp}	$\sim$ 13 ms
$t_{at\ pressure}$	$\sim$ 16ms

Table 8.4: List of times for each step within the cycle.

file name	**description**
RH_meas_i.csv	monitoring the RH for one measurement i
conc_meas_i.csv	monitoring the concentration for measurement i
DAQPT.txt	monitoring the room temperature and the pressure for the hole day
j.MND	output file of an evaluated SANC measurement. j is the number of different pressure values.
Ej	output file for the experimental growth data
Tj	output file of the calculated growth data

Table 8.5: Summary of the acquired data files for each measuring day. i=1,2,3 indicates the first/second or third measurements performed on one day. j is the number of measurements at different pressure values that were performed. This value corresponds to the number of points in the activation curve. For the growth calculation measurements where the plateau was reached were taken.

description	name	resolution	range/limitation
humidity sensor	SHT75 [90]	± 1.8% ± 4%	<90% >90%
tube furnace	Nabertherm R50/250/13 [107]	± 5K	T_{max} = 1300K
DMA	Vienna-type DMA	β; eq.(3.5)	0 - 10 000V
CPC	UCPC Model 3776 [75]	± 10%	< $3{\cdot}10^5$ /cm^3
FCE	Aerosol Electrometer Model 3068 [78]	±1fA	±12 500fA
chiller	Lauda RM6 [83]	± 0.3°C	-20 - 100 °C
	Lauda RK20 [84]	± 0.1°C	-40 - 150 °C
	Lauda VC Vario Cool [85]	± 0.05 °C	-20 - 80°C
SANC	SANC	S ± 3%	
charger	TSI Advanced Aerosol Neutralizer 3088	f_c; eq.(3.1)	0,3 - 5lpm [108]

Table 8.6: List of instrumentation with their specifications.

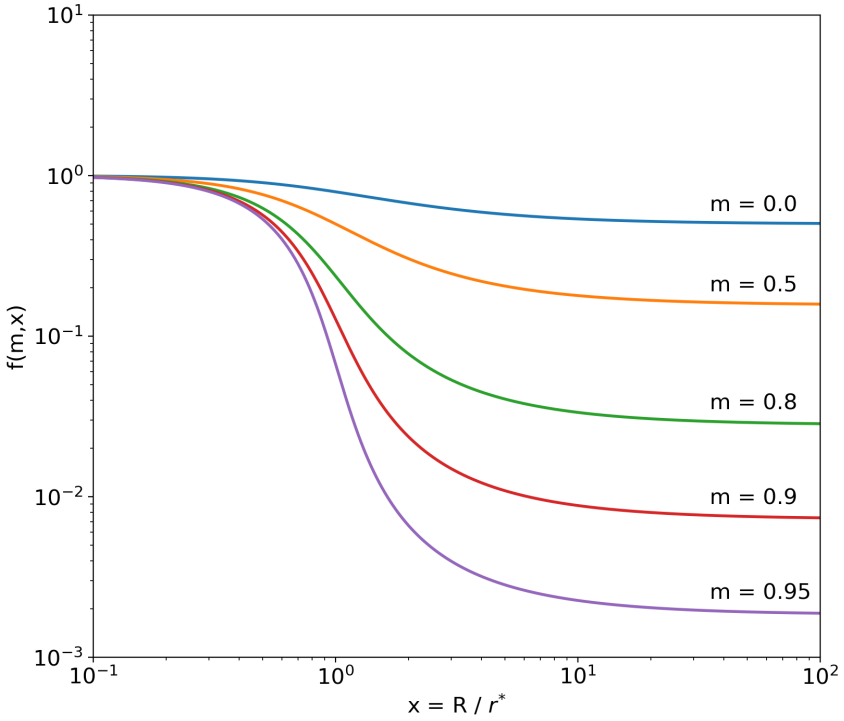

Figure 8.1: Based on Fletcher's theory which discusses the nucleation of vapor on a spherical surface with Radius R [109]. The plot shows the form factor as a function of x and m, see eq.(8.1). x is the ratio between the radius of the spherical surface (seed particle) and the critical radius r* and m is the contact parameter (m = cos(θ), with θ being the contact angle). Considering Fletcher's form factor, the energy barrier introduced in eq.(2.17) is extended to eq.(8.2). Therefore a higher ratio between the seed particle size and the critical cluster size leads to a smaller form factor. Furthermore, a smaller form factor decreases the energy barrier, see eq.(8.2).

$$f(m,x) = \frac{1}{2}\left\{1 - \left(\frac{mx-1}{g}\right)^3 + x^3\left[2 - 3\left(\frac{x-m}{g}\right) + \left(\frac{x-m}{g}\right)^3\right] + 3mx^2\left(\frac{x-m}{g} - 1\right)\right\}$$
$$g = \sqrt{1 + x^2 - 2mx} \tag{8.1}$$

$$\Delta G^{het*} = f(m,x) \cdot \Delta G^{hom*} \tag{8.2}$$